

Side View of Rockfall Blocks with Drift

Perspective View of Rockfall Blocks with Drift

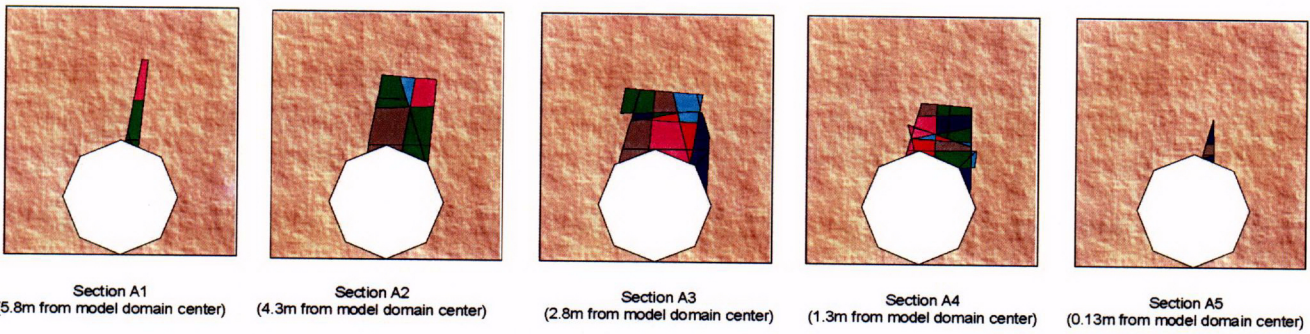


Figure 101. Drift Profile for  $1 \times 10^{-7}$  Hazard Level, Worst Case

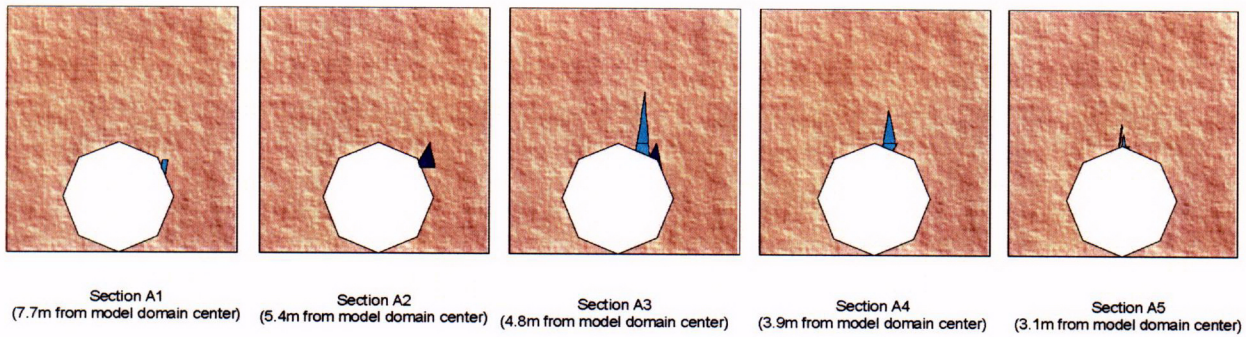
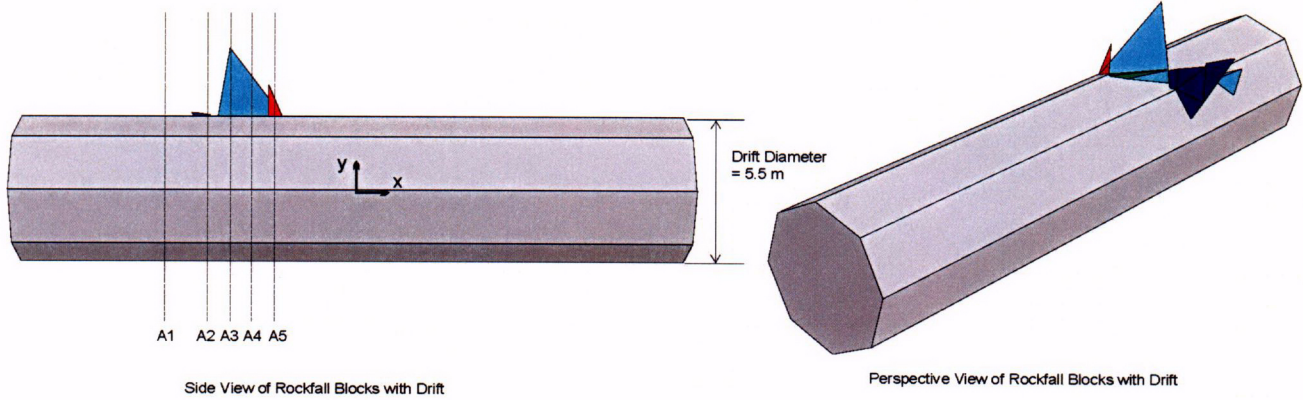
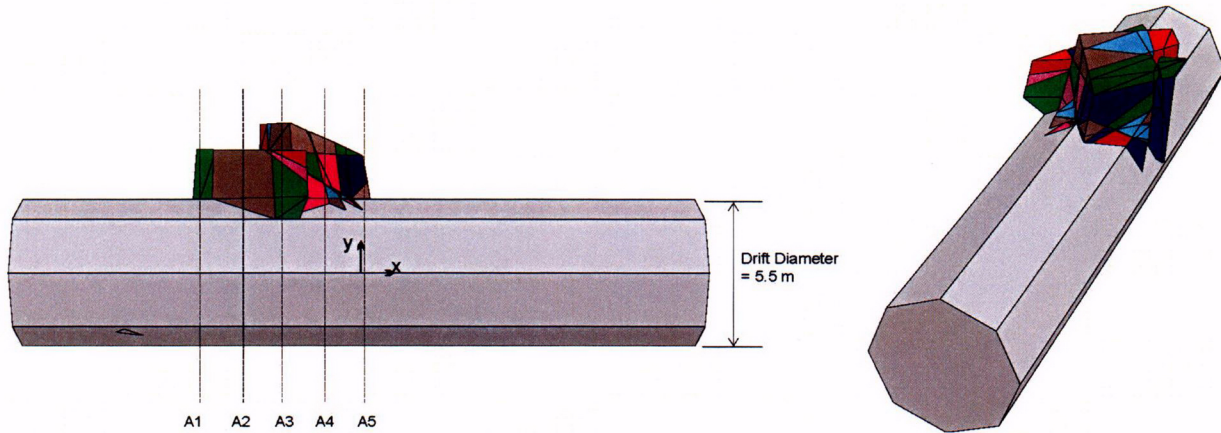


Figure 102. Drift Profile for  $1 \times 10^{-7}$  Hazard Level, 75 Percentile Case



Side View of Rockfall Blocks with Drift

Perspective View of Rockfall Blocks with Drift

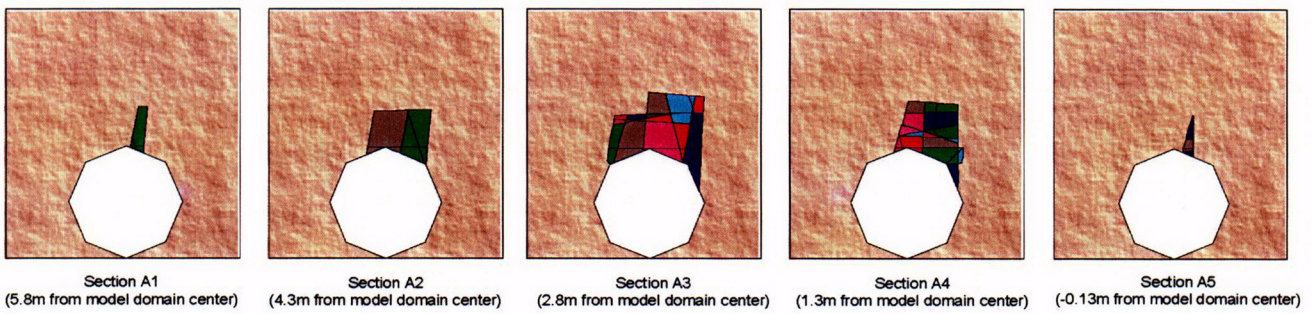


Figure 103. Drift Profile for  $1 \times 10^{-6}$  Hazard Level, Worst Case

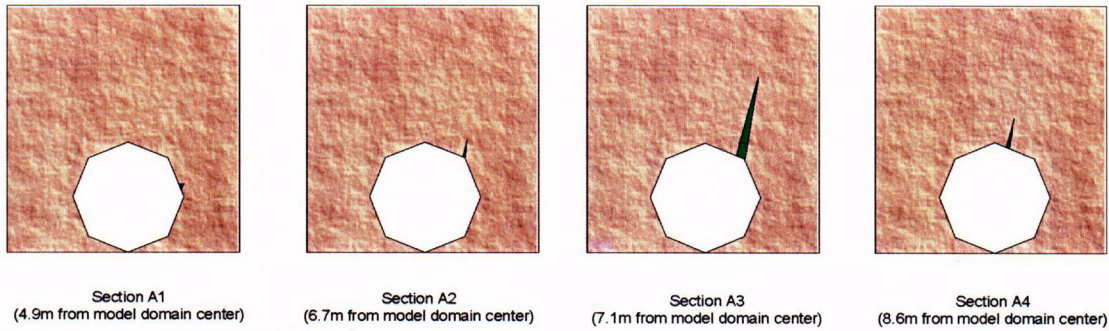
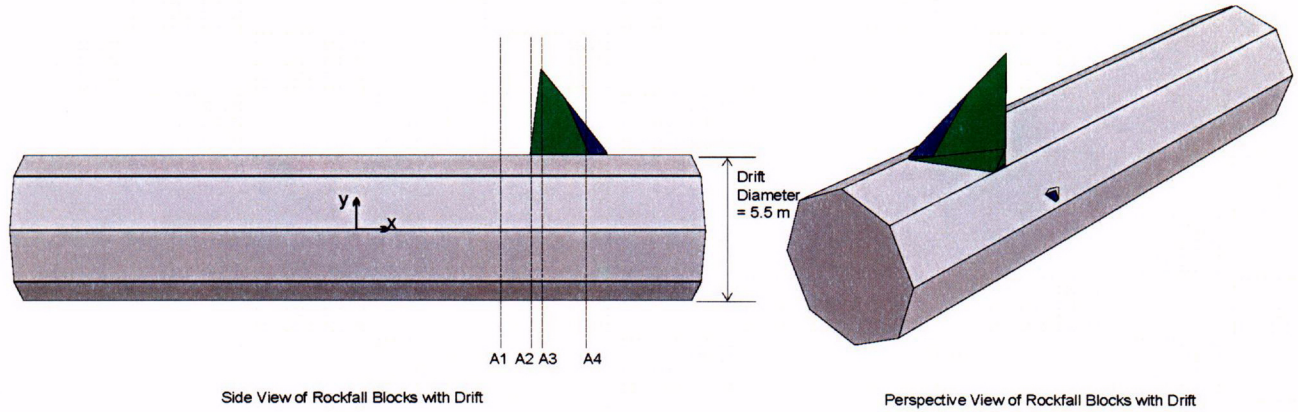


Figure 104. Drift Profile for  $1 \times 10^{-6}$  Hazard Level, 75 Percentile Case

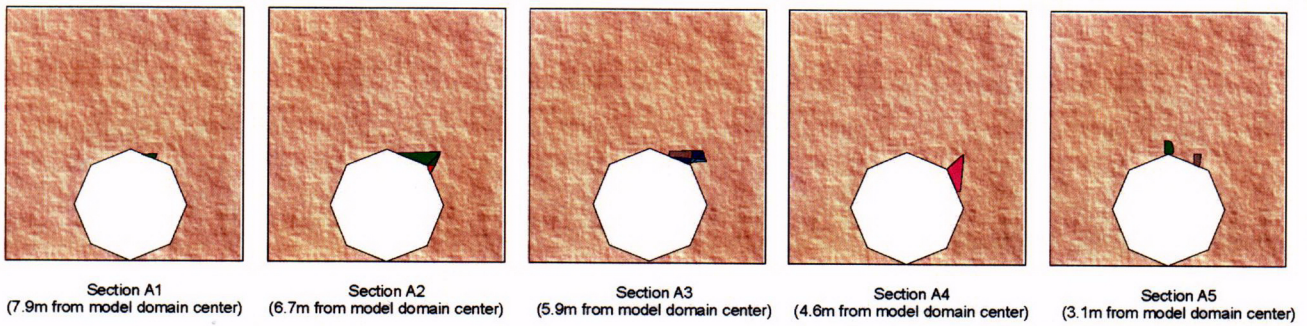
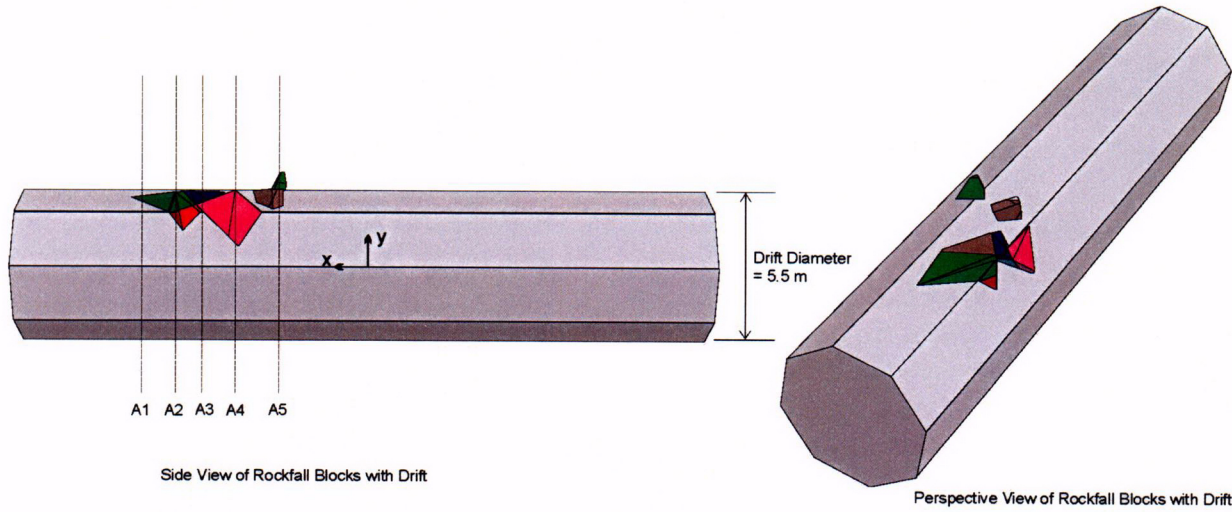


Figure 105. Drift Profile for  $5 \times 10^{-4}$  Hazard Level, Worst Case

Table 33. Predicted Number of Rockfall and Volume for the Presented Drift Profile

Simulation	Number of Blocks	Total Volume (m <sup>3</sup> )
1×10 <sup>-7</sup> hazard, worst case profile	46	50.64
1×10 <sup>-7</sup> hazard, 75 percentile profile	5	2.02
1×10 <sup>-6</sup> hazard, worst case profile	44	42.26
1×10 <sup>-6</sup> hazard, 75 percentile profile	3	1.06
5×10 <sup>-4</sup> hazard, worst case profile	14	3.03

#### 6.4 ROCKFALL IN THE LITHOPHYSAL UNITS

Lithophysal units, particularly the lower lithophysal (Ttptll), are characterized by intense fracturing. Joint sets are not as clearly defined as in middle nonlithophysal (Ttptmn) units. Average joint spacing is less than 1 m, and at certain locations this spacing is much smaller, in the order of 0.1 m (as discussed in Section 6.1.4.1). In addition to fracturing on different scales, lithophysal rock mass is characterized by the presence of almost uniformly distributed holes (lithophysae) of varying size (from less than 1-cm to 1-m in diameter). The lithophysae account for up to 30 percent of the rock mass volume (see Section 6.1.4.2 for a detailed discussion on lithophysae). The size of the internal lithophysae structure and fracture spacing is much smaller than the drift size (i.e., 5.5-m diameter). There is no preferred direction in the orientation that would justify introduction of anisotropy. Heterogeneity is considered on the scale of the repository in such a way that the analysis on the drift scale is conducted using different properties of the rock mass to investigate the effect of varying quality of rock mass on drift stability. However, properties within each model are considered homogeneous. Under such conditions, when there is no internal structure in the model, and properties are isotropic and homogeneous, the drift stability analysis is conducted using a two-dimensional model in the plane perpendicular to the drift axis. The model results of rockfall prediction in the lithophysal units (in a cross-section characterized by particular rock mass properties) can be used to provide an estimate of overall rockfall in the lithophysal zone based on the distribution of different rock mass qualities throughout the repository.

The assessment of rock mass properties for lithophysal rock is documented in Attachment V (Section V.4.1). Six categories were developed to represent the range of rock mass properties as summarized in Table 34. The validity of this approach to represent the lithophysal rock mass is discussed in Sections 7.3 and 7.4. Categories 1 through 5 represent variability of rock mass quality throughout the repository level. Category 6 was considered as extremely poor quality of rock on the repository level used for very conservative (i.e., high) predictions of damage and rockfall.

Table 34. Categories of the Lithophysal Rock Mass Selected for Analysis

Category	Unconfined Compressive Strength (MPa)	Estimated Young's Modulus (GPa)	Bulk Modulus, K (GPa)	Shear Modulus, G (GPa)
1	10	1.9	1.07	0.80
2	15	6.4	3.54	2.65
3	20	10.8	6.01	4.51
4	25	15.3	8.48	6.36
5	30	19.7	10.95	8.21
6	6	1.0	0.56	0.42

NOTE: The calculation of rock strength properties is documented in Attachment V (Section V.4.1).

#### 6.4.1 Two-Dimensional Discontinuum Analysis of Lithophysal Rock Mass

The objective of the analysis presented in this section is to predict the amount of rockfall in the emplacement drifts due to: (a) drift excavation, (b) stresses induced by the heat released by the waste, (c) seismic ground motions with different probabilities of occurrence, and (d) strength degradation. The standard approach in geotechnical engineering of solving problems of stability of underground excavation is using models based on continuum mechanics. Such an approach is quite effective if the main interest is stress redistribution around an opening or displacements. However, difficulties are encountered if a continuum model is used for prediction of instability. Continuum models use constitutive models to describe the mechanical behavior of a material. A linearly elastic-perfectly plastic Mohr-Coulomb constitutive model is often used to represent mechanical behavior of a rock mass. Because the material strength of a perfectly plastic Mohr-Coulomb model does not decrease as a function of plastic deformation, the model of a drift will show indications of material yielding (i.e., plastic deformation) in different portions of the model, but will never actually predict the rockfall. It is necessary to use a strain-softening constitutive model, in which strength degrades as a function of deformation after the peak-strength of material has been reached, to have a reasonable prediction of rockfall area. However, the strain-softening model within the framework of continuum mechanics leads to problems of mesh dependency. It was decided, based on all previous considerations, to use the two-dimensional distinct element code, UDEC (Section 3.1), for drift stability analysis. In the UDEC model, the rock mass is represented as an assembly of polygonal, elastic blocks. The entire domain is discretized into blocks using Voronoi tessellations (Itasca 2002). The joints between blocks are considered to be linearly elastic-brittle. The joints between the blocks represent the pre-existing fractures. The elastic behavior of joints is controlled by normal and shear stiffness (joint stiffness is constant). Joints can sustain finite tensile stress as prescribed by tensile strength. The Coulomb slip condition governs the onset of slip as a function of joint cohesion and friction angle. If a joint fails either in tension or shear, tensile strength, friction and cohesion are reset to residual values. This model allows for the formation of joints between blocks, separation and instability (under action of gravity) of portions of rock mass around a drift. No ground support was considered in the analyses. All cases of thermal and seismic loading considered in this section were also analyzed using a continuum, linearly elastic approximation. The analyses were done using the finite difference code FLAC (Section 3.1). The results of the continuum model were used as a reference for easier interpretation of the results from the complex UDEC model.

## Drift Degradation Analysis

Additional details for the justification and calibration of the lithophysal rock model are provided in Section 7.7. The calibrated micro properties are listed in Tables 35 and 36, for UDEC models with average block sizes of 0.2 m and 0.3 m, respectively. Note that, if not indicated otherwise, the analysis was done using a block size of 0.3 m.

The geometry of the UDEC model is shown in Figure 106. As indicated, only the region around the drift where inelastic deformation is expected is discretized into Voronoi blocks. The rest of the model is composed of a few large, elastic blocks. However, the resulting stiffness of the discretized portion of the model (i.e., stiffness of blocks and joints together) is the same as the stiffness of the large elastic blocks, which represent far-field behavior.

Table 35. Micro Properties in the Model with 0.2 m Block Size

Category	Friction Angle (deg)	Residual Friction Angle (deg)	Cohesion (MPa)	Tension (MPa)	Normal Stiffness (GPa/m)	Shear Stiffness (GPa/m)	Block Bulk Modulus (GPa)	Block Shear Modulus (GPa)
1	35	15	3.91	1.56	13.40	6.69	13.00	9.75
2	35	15	5.86	2.34	45.10	22.50	43.60	32.80
3	35	15	7.82	3.12	76.20	38.00	73.60	55.40
4	35	15	9.77	3.90	108.00	53.90	104.00	78.50
5	35	15	11.70	4.68	139.00	69.40	134.00	101.00
6	35	15	2.34	0.94	7.05	3.52	6.82	5.13

NOTE: Residual cohesion and tensile strength are zero.

Table 36. Micro Properties in the Model with 0.3 m Block Size

Category	Friction Angle (deg)	Residual Friction Angle (deg)	Cohesion (MPa)	Tension (MPa)	Normal Stiffness (GPa/m)	Shear Stiffness (GPa/m)	Block Bulk Modulus (GPa)	Block Shear Modulus (GPa)
1	35	15	3.83	1.53	9.34	4.67	9.03	6.80
2	35	15	5.85	2.34	31.48	15.72	30.44	22.88
3	35	15	7.94	3.18	53.08	26.57	51.37	38.60
4	35	15	10.09	4.03	74.90	37.60	72.80	54.70
5	35	15	12.30	4.92	97.00	48.40	93.60	70.50
6	35	15	2.30	0.92	4.90	2.50	4.80	3.60

NOTE: Residual cohesion and tensile strength are zero.

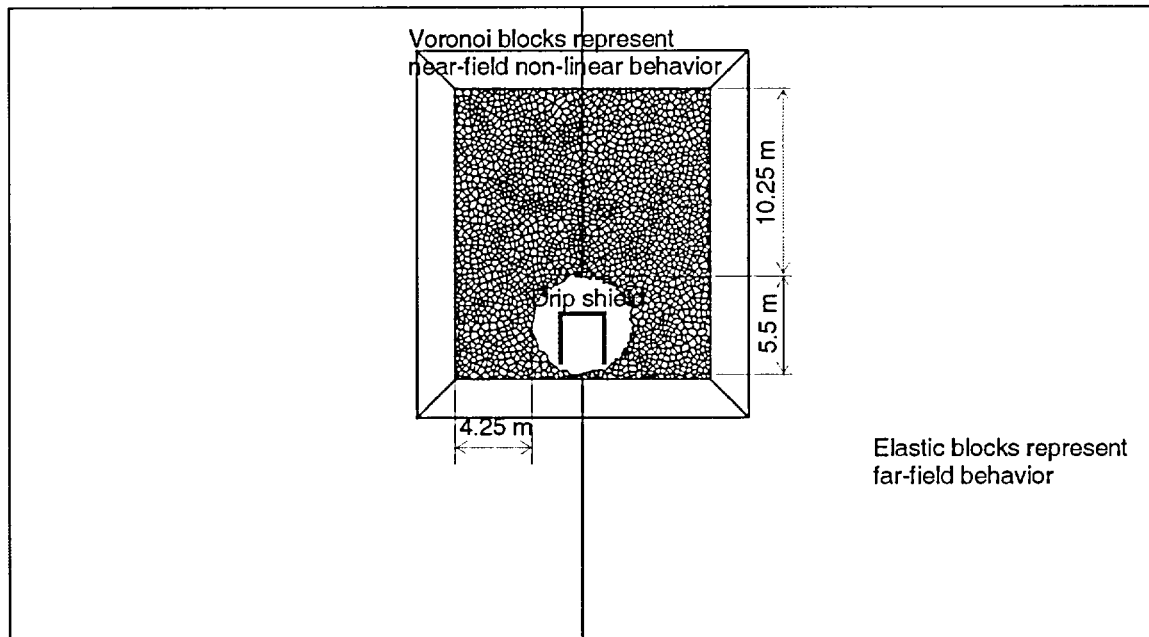


Figure 106. Geometry and Initial Conditions of the UDEC Model

#### 6.4.1.1 Seismic Consideration in Lithophysal Units

Drift stability was analyzed for different conditions of ground motion:

- Ground motion with  $5 \times 10^{-4}$  probability of annual occurrence (preclosure earthquake, DTN: MO0211TMHIS104.002)
- Ground motion with  $1 \times 10^{-6}$  probability of annual occurrence (postclosure earthquake, DTN: MO0301TMHIS106.001).

The ground motions are discussed in detail in Section 6.3.1.2.1. Fifteen ground motions (two horizontal and one vertical component of motion) were considered in the analysis for  $1 \times 10^{-6}$  probability of annual occurrence. Only one ground motion was considered for  $5 \times 10^{-4}$  probability of annual occurrence. Instead of simulating all possible combinations of the 15 cases of ground motion (for  $1 \times 10^{-6}$  probability) with six rock mass categories, only 15 realizations shown in Table 37 were simulated (note that 15 ground motions are numbered 1 through 14 in sequence, and 16). Based on Latin Hypercube sampling (DTN: MO0301SPASIP27.004), realizations from Table 37 are selected as representative of all possible realizations. Combinations in Table 37 include only rock mass categories 1 through 5, as representative of variability of lithophysal rock mass quality on the repository level. Only postclosure ground motion number 1 was considered for rock mass category 6 as an extreme condition. It was planned to conduct simulations of drift stability for ground motions with  $1 \times 10^{-7}$  probability of annual occurrence. However, the results of analyses for  $1 \times 10^{-6}$  probability of annual occurrence (complete collapse of the emplacement drifts) proved such an analysis futile. Because there is just one preclosure ground motion case, it was analyzed for all six rock mass categories.

Drift Degradation Analysis

Table 37. Simulated Combinations of  $10^6$  Ground Motions and Rock Mass Categories

Realization Number	Ground Motion Time History Number	Rock Mass Category Number
1	4	3
2	8	5
3	16	4
4	12	1
5	2	3
6	8	1
7	14	2
8	4	4
9	10	2
10	6	3
11	9	1
12	1	1
13	1	3
14	7	4
15	11	4

DTN: MO0301SPASIP27.004

NOTES: Realization numbers 1 through 15 are from the sampling in the lithophysal zone provided by the source DTN.

An in situ (before excavation) stress state, defined by 7 MPa vertical and 3.5 MPa horizontal stresses, is used throughout the simulations, which is consistent with the 3DEC modeling in Section 6.3. The equilibrium state of the model after excavation of a drift represents the initial condition for the dynamic analysis. This equilibrium state is achieved by performing quasi-static simulation. The geometry and the boundary and initial conditions used in the initial quasi-static simulation preceding the dynamic simulation are illustrated in Figure 107.

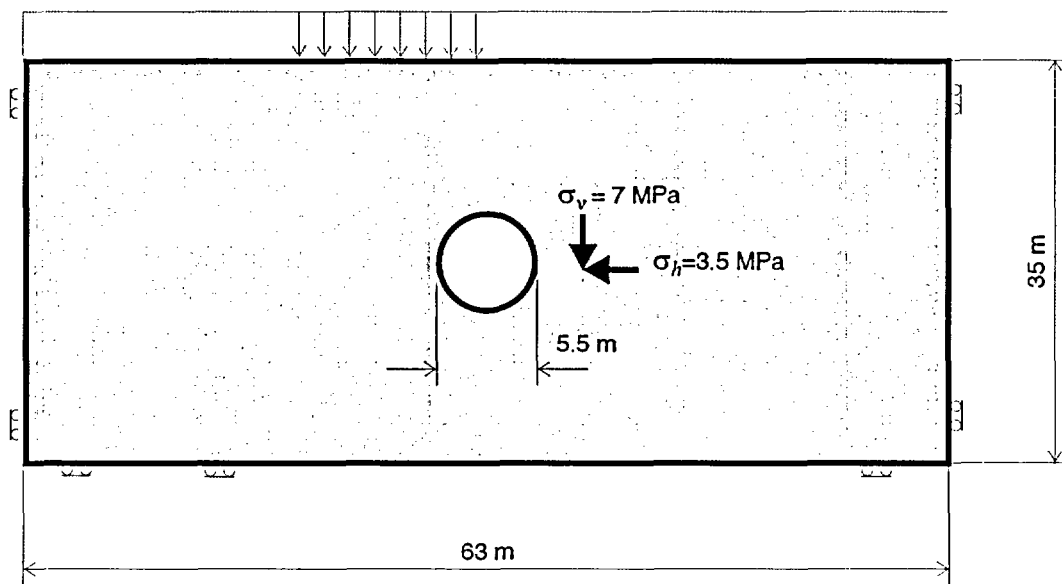


Figure 107. Dynamic Model, Initial and Boundary Conditions: Initial Static Simulation

The boundary conditions as used in the dynamic analysis are illustrated in Figure 108. Quiet boundaries (indicated in Figure 108 as viscous boundaries) were used on all models outside boundaries. These boundaries prevent reflection of outgoing seismic waves back into the model. Quiet boundaries were combined with free-field boundaries on the vertical outside boundaries. The free-field boundaries perform one-dimensional simulation of vertically propagating plane waves representing motion of truncated, semi-infinite medium. They prevent distortion of vertically propagating plane waves along the quiet boundaries. Dynamic loading was applied at the bottom of the model, as propagating vertically upwards. Although the dynamic loading was specified as velocity histories, it was applied at the bottom model boundary as stress boundary condition. However, using formulas developed for plane waves in elasto-dynamics, direct relation between velocity and stress can be established (Itasca 2002, Manuals/3DEC/Optional Features/Section 2: Dynamic Analysis, Section 2.6):

$$\begin{aligned} \sigma_y &= 2\rho C_p v_v \\ \sigma_{xy} &= 2\rho C_s v_h \end{aligned} \tag{Eq. 7}$$

where  $\rho$  is material density;  $C_p$  and  $C_s$  are P and S wave velocity; and  $v_v$  and  $v_h$  are vertical and horizontal velocity component. The factor 2 in Equation 7 is due to quiet boundaries. Figure 109 shows specified component 1 of the horizontal velocity history for ground motion 14. Velocity histories at the bottom and the top of the model, also shown in Figure 109, recorded during the simulation, confirm that the applied stress boundary condition results into the motion, which is exactly the same as the specified velocity boundary condition. Comparison of the velocities at the top and the model (identical histories slightly offset in time) confirms that the free-field boundaries operate correctly.

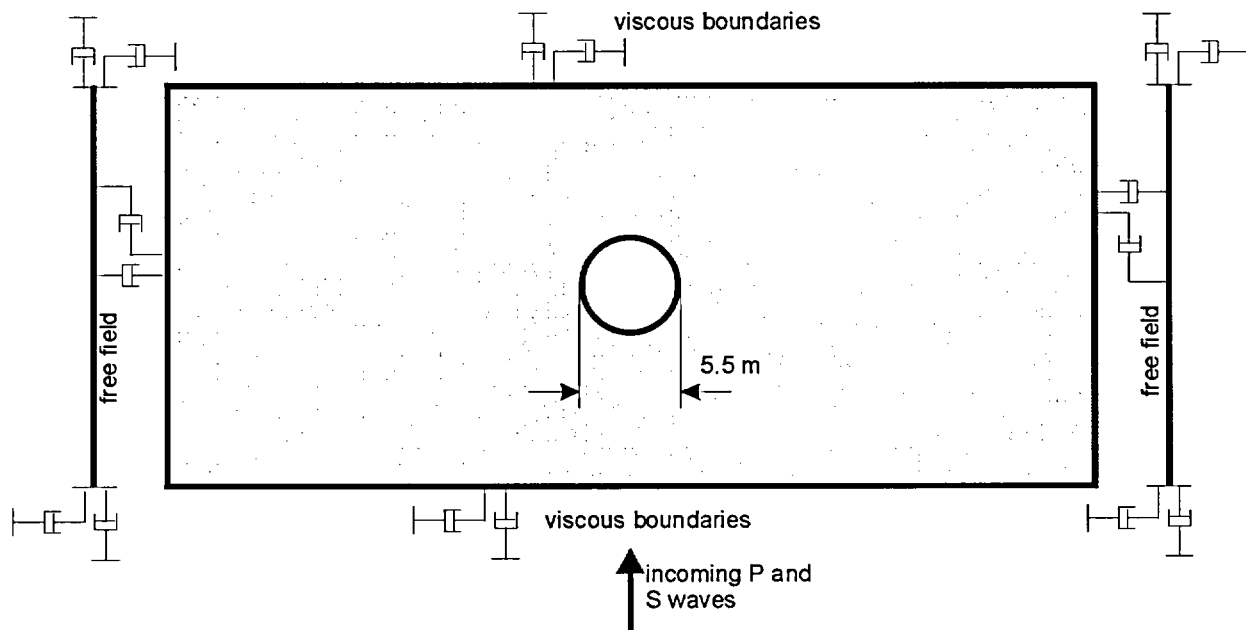
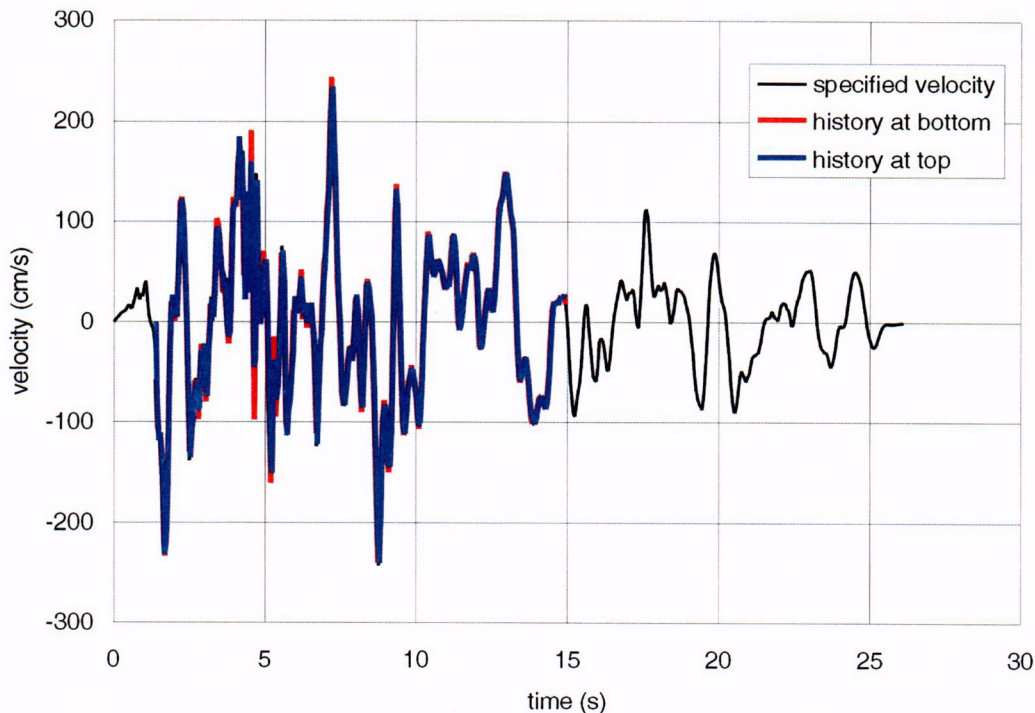


Figure 108. Dynamic Model Boundary Conditions for Dynamic Simulation

Drift Degradation Analysis

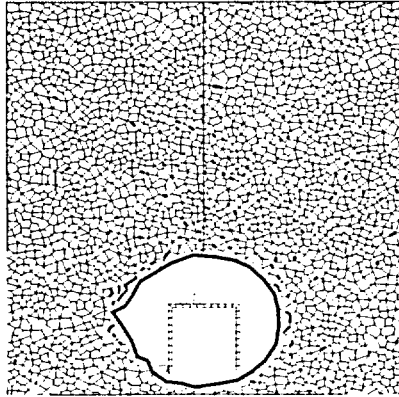


NOTES: The specified horizontal velocity is provided by DTN: MO0301TMHIS106.001. The horizontal velocities recorded at the top and at the bottom of the model coincide with the specified velocity.

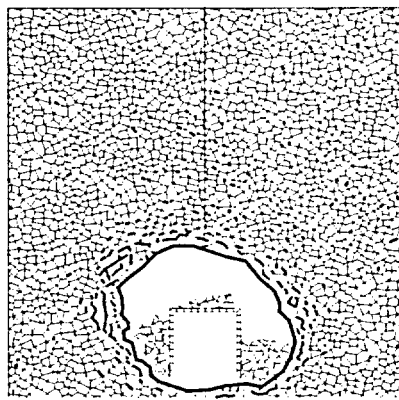
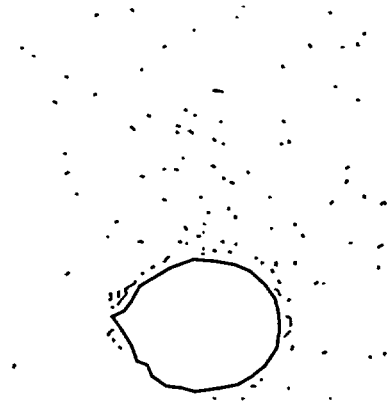
Figure 109. Horizontal Velocity, Component 1 for Ground Motion 4

The conducted analyses indicate that ground motion with a probability of an annual occurrence of  $5 \times 10^{-4}$  will not induce any rockfall for rock mass categories 2 through 5. A relatively small amount of rockfall from the drift walls (shown in Figure 110a) is expected for category 1. The amount of rockfall and fracturing of the surrounding rock mass for extremely poor quality of rock (category 6), assuming no ground support, is shown in Figure 110b. The elastic stress paths from the preclosure ground motion simulation for the category 1 rock mass (shown in Figures 111 and 112 in the wall and roof, respectively) and the category 5 rock mass (shown in Figures 113 and 114 in the wall and roof, respectively) indicate that this level of ground motion causes small oscillations of the stress state relative to the initial equilibrium. With the exception of the point on the drift wall located in the category 1 rock mass, all stress states are within the elastic region throughout the duration of the preclosure ground motion. The observed rockfall is a consequence of regions that are above the yield limit after excavation of the drift (i.e., the wall in the category 1 rock mass) being shaken down.

Drift Degradation Analysis



a) category 1



b) category 6

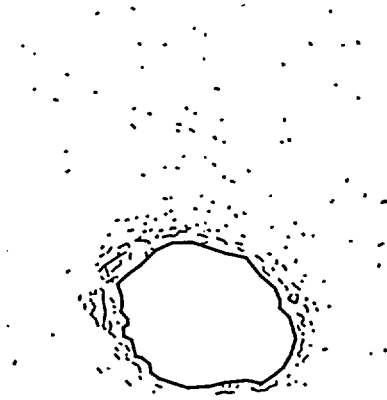


Figure 110. Geometry of the Model after Simulation for Preclosure Ground Motion (Probability  $5 \times 10^{-4}$ ):  
Rock Mass Categories 1 and 6

Drift Degradation Analysis

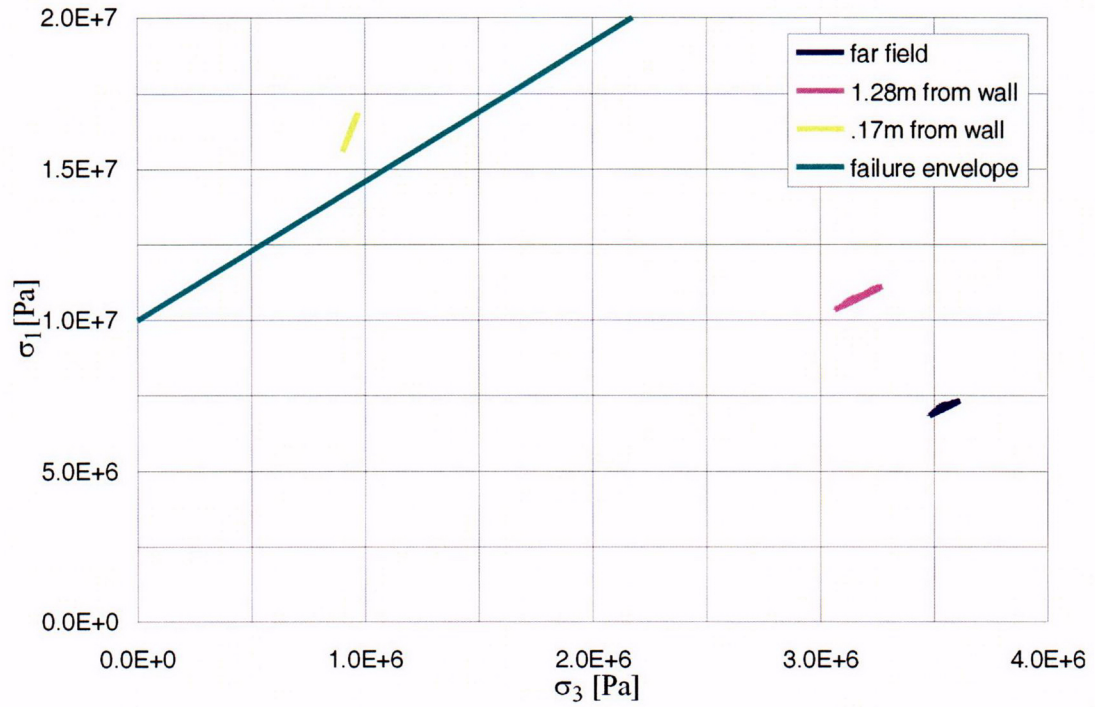


Figure 111. Elastic Stress Paths in the Drift Wall due to Preclosure Ground Motion: Category 1

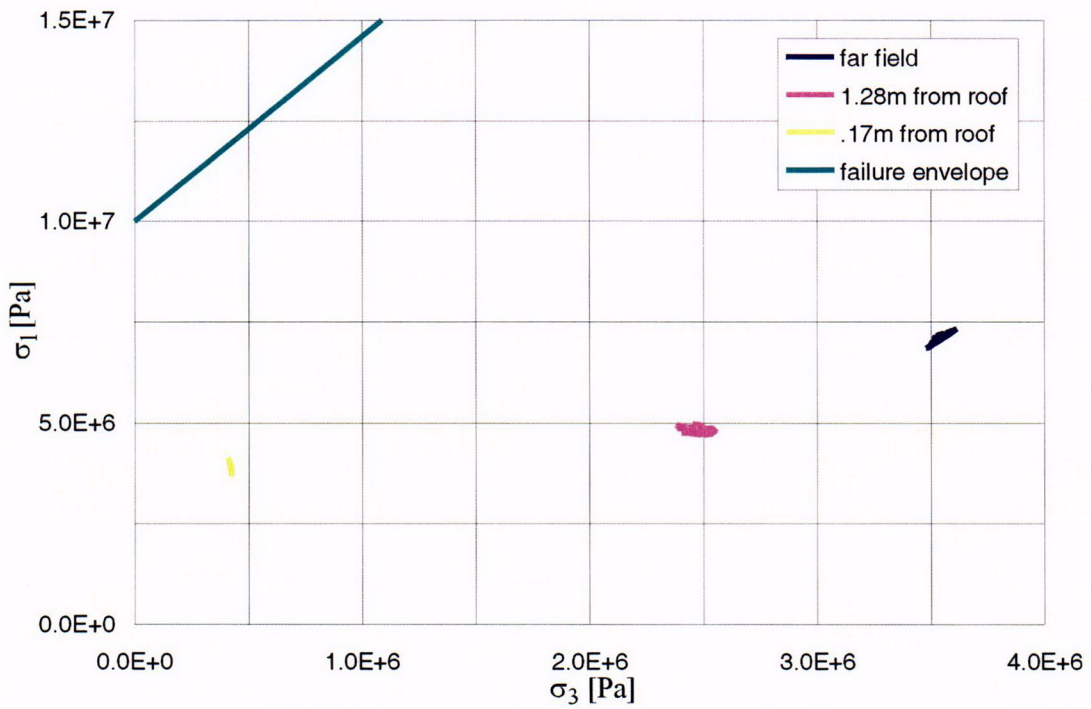


Figure 112. Elastic Stress Paths in the Drift Roof due to Preclosure Ground Motion: Category 1

Drift Degradation Analysis

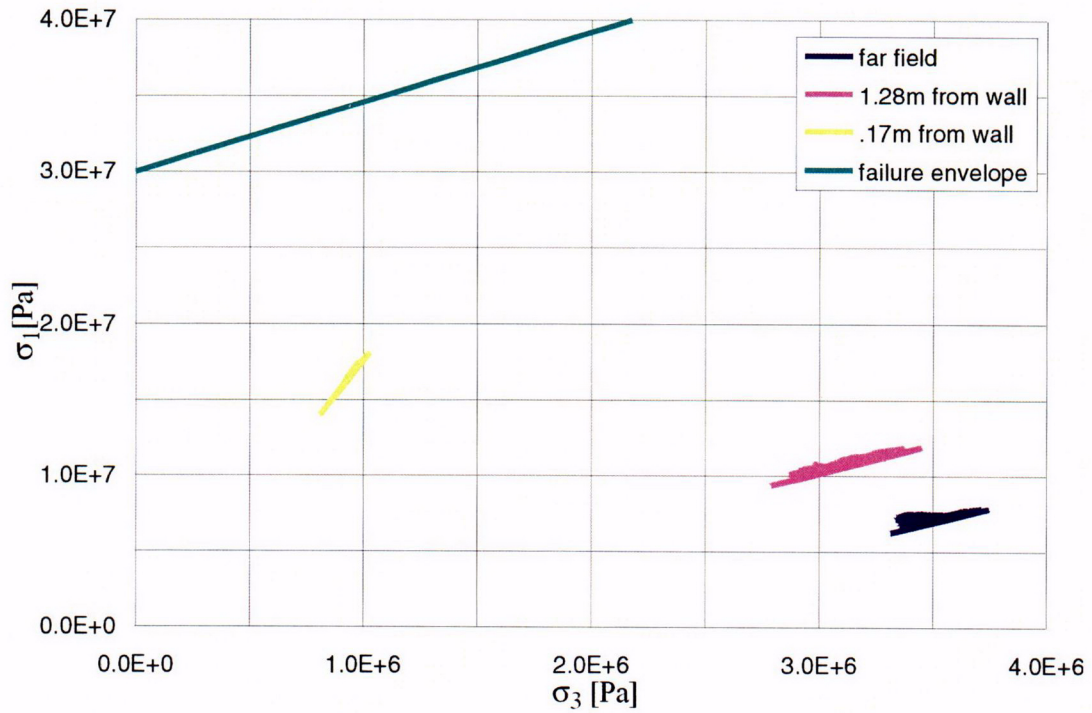


Figure 113. Elastic Stress Paths in the Drift Wall due to Preclosure Ground Motion: Category 5

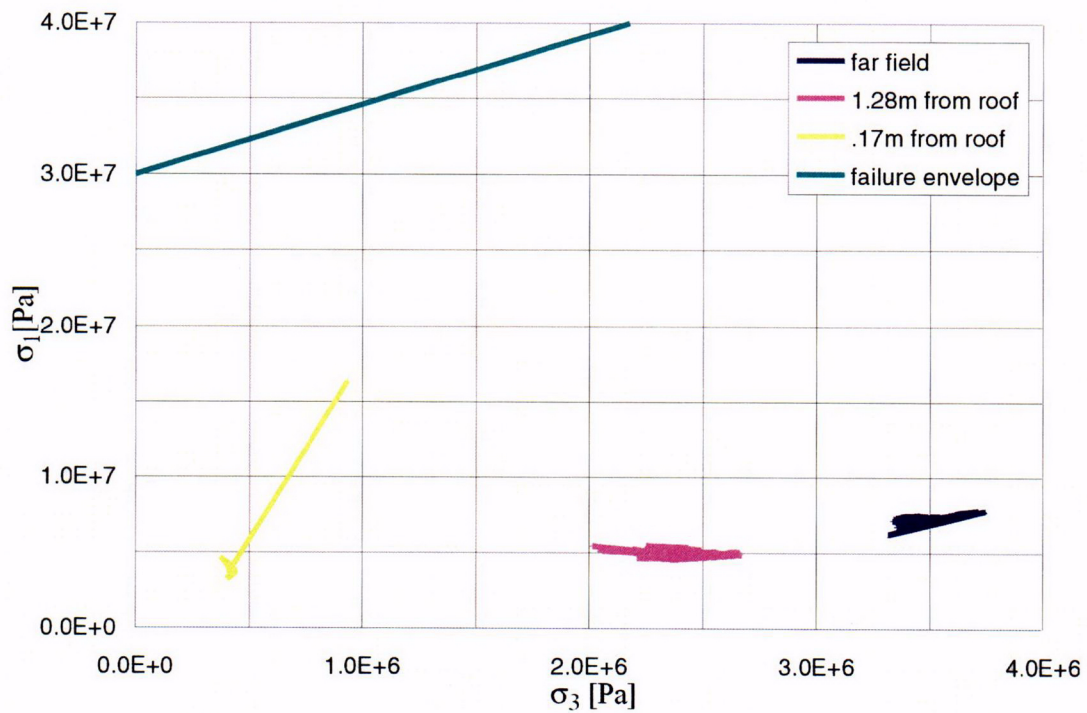


Figure 114. Elastic Stress Paths in the Drift Roof due to Preclosure Ground Motion: Category 5

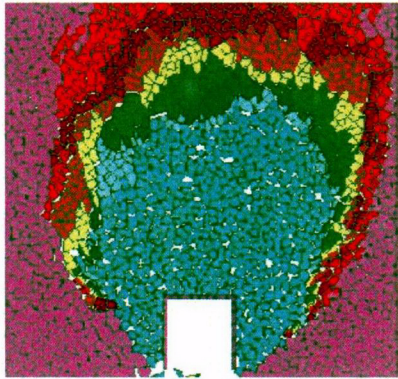
Ground motions with a probability of an annual occurrence of  $1 \times 10^{-6}$  cause complete collapse of the emplacement drifts irrespective of the rock mass category and ground motion case. The model geometries after simulations of realization numbers 1 through 6 from Table 37 are shown in Figure 115. Elastic stress paths (for ground motion case 1) shown in Figures 116 and 117, for the category 1 rock mass, and Figures 118 and 119, for the category 5 rock mass, demonstrate different mechanisms of drift collapse depending on the rock mass quality. In poor quality rock masses (e.g., categories 1 and 6), far-field stress (unaffected by the drift) is mostly elastic during the history of the ground shaking. However, stress amplifications and concentrations around the drift cause intense yielding in tension and shear, which eventually causes the drift to collapse. In the case of better rock mass quality (e.g., category 5), the rock mass fails in the tension even for far-field conditions (away from the drift), and tensile fractures propagate throughout the rock mass. The drift creates an open space into which the loose blocks collapse.

After the drift collapses, the overall bulking of the collapsed material in the model causes complete closure of the drift opening. The resulting pressures of the caved rock mass on the top, left and right side of the drip shield are summarized in Table 38. Detailed results for drip shield pressures are provided in Attachment XVI. The extremely large pressure ( $507.1 \text{ kN/m}^2$ ) on the right side of the drip shield for realization number 10 is a model artifact due to a single block wedged between the lower edge of the drip shield (set as rigid in the analysis) and the still unbroken rock mass. In reality, blocks are not elastic and such a stress would cause its breakage. Deformation of the drip shield would also result in a reduction of lateral pressure.

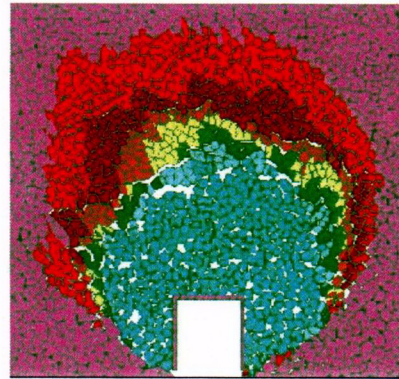
#### 6.4.1.2 Thermal Consideration in Lithophysal Units

Geometry and boundary conditions used in the model for predictions of thermally induced rockfall are shown in Figure 120. The model does not perform complete thermal-mechanical simulation. Instead, temperature fields calculated with the code NUFT, for  $1.45 \text{ kW/m}$  and 50 years of forced ventilation, are imported into UDEC (thermal calculation described in Section 6.2). Two cases of ventilation efficiency were considered: 90 and 70 percent. Stresses are calculated for each new temperature state based on the temperature increment (from the previous temperature state) and the coefficient of thermal expansion. For all considered cases, the same coefficient of thermal expansion, function of temperature, was used. In order to have gradual evolution of stresses during the simulated time, 45 temperature fields (corresponding to different times after waste emplacements) were considered. For each new temperature field, simulation was conducted in two steps. First, the model was run to the equilibrium elastically (i.e., all unbroken bonds were made infinitely strong). Next, after the model had reached equilibrium, the actual strength was assigned to the unbroken bonds and the model was run again to the equilibrium. The reason for the two-step approach was to reduce the impact of non-gradual stress changes due to incremental changes of temperature state. The entire analysis was conducted considering that rock mass strength does not degrade with time. Any observed damage and rockfall are consequences of the thermally induced stresses only. All three cases of thermal calculation (described in Section 6.2) were considered for the drift stability analysis in lithophysal rock mass: (a) base case (average thermal properties and 90 percent ventilation efficiency); (b) case 2, sensitivity calculation for thermal properties (thermal properties one standard deviation smaller than the average properties); and (c) case 3, sensitivity calculation for the heat removal ratio (average thermal properties and 70 percent ventilation efficiency).

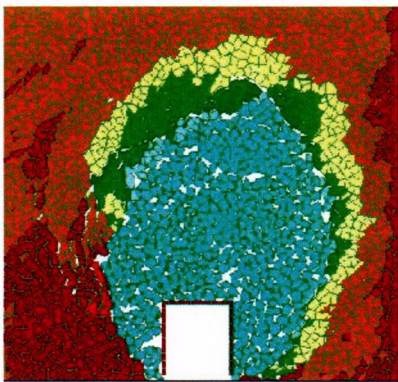
Drift Degradation Analysis



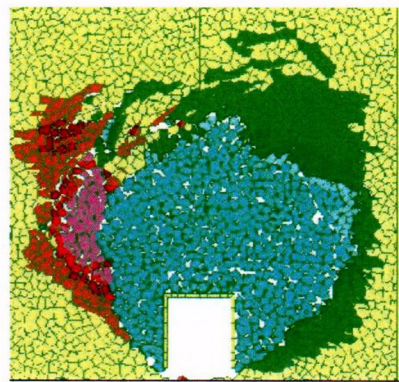
a) realization 1



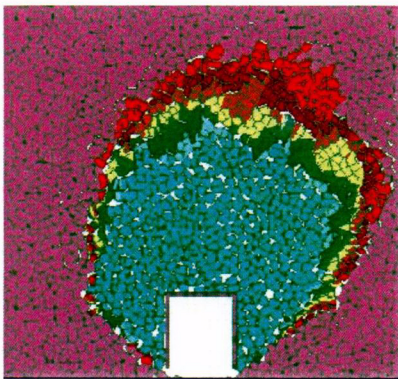
b) realization 2



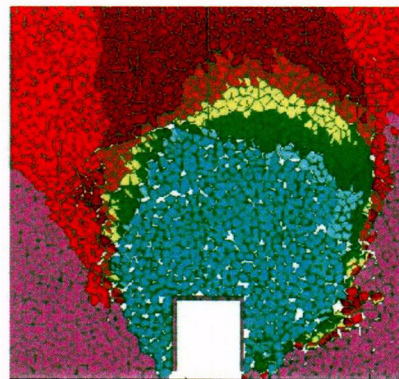
c) realization 3



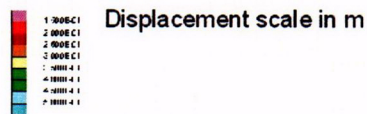
d) realization 4



e) realization 5



f) realization 6



NOTE: Blocks are colored by magnitude of displacement.

Figure 115. Geometry of the Model after Simulations for Postclosure Ground Motions (Probability  $1 \times 10^{-6}$ ): Realizations 1 through 6 from Table 37

Drift Degradation Analysis

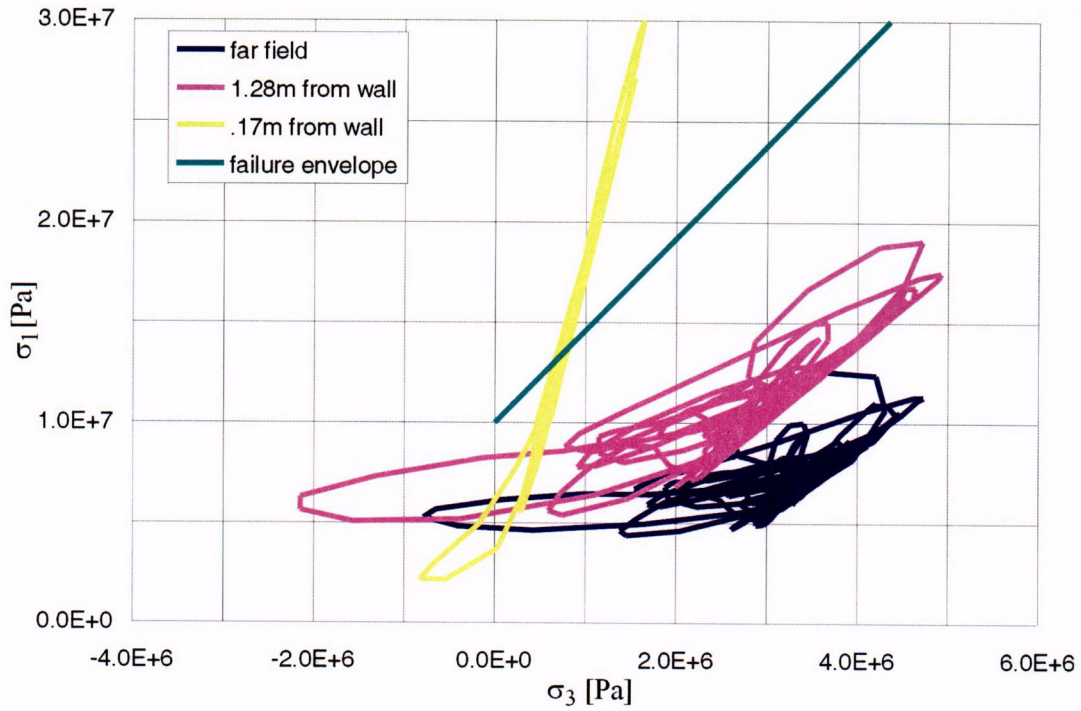


Figure 116. Elastic Stress Paths in the Drift Wall due to Postclosure Ground Motion No. 1: Category 1

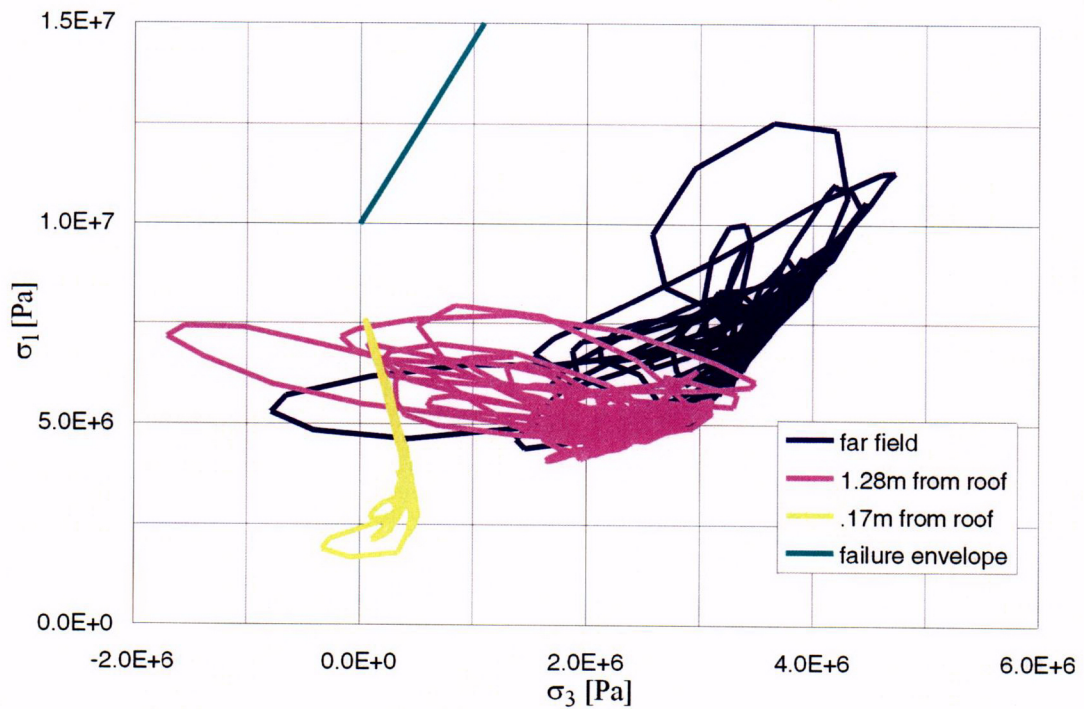


Figure 117. Elastic Stress Paths in the Drift Roof due to Postclosure Ground Motion No. 1: Category 1

# Drift Degradation Analysis

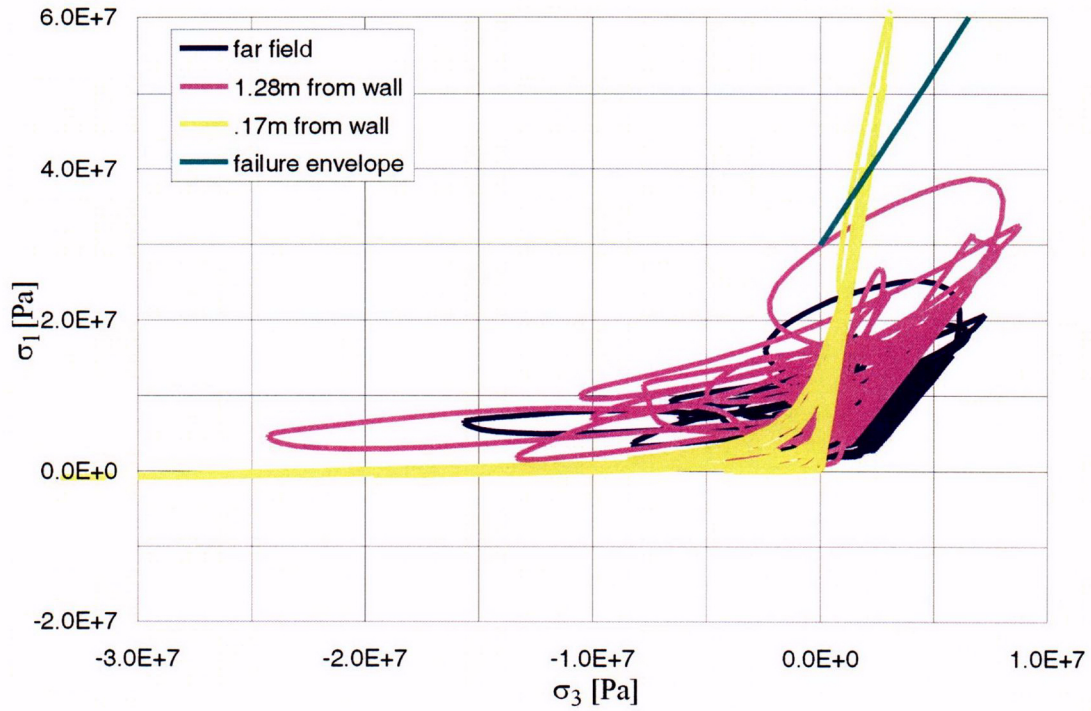


Figure 118. Elastic Stress Paths in the Drift Wall due to Postclosure Ground Motion No. 1: Category 5

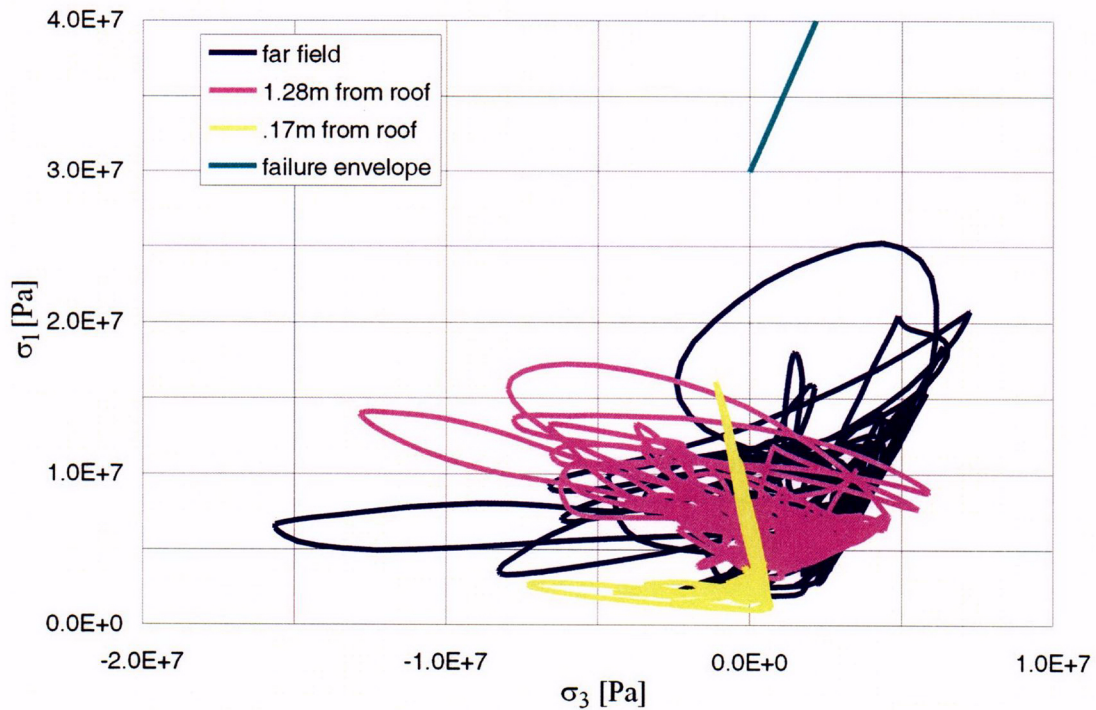


Figure 119. Elastic Stress Paths in the Drift Roof due to Postclosure Ground Motion No. 1: Category 5

Drift Degradation Analysis

Table 38. Summary of Loads on the Drip Shield after Drift Collapse Caused by Postclosure Ground Motion (Probability  $1 \times 10^{-6}$ )

Realization Number	Pressure Left (kN/m <sup>2</sup> )	Pressure Top (kN/m <sup>2</sup> )	Pressure Right (kN/m <sup>2</sup> )	Bulking (kN/m <sup>2</sup> )
1	33.0	263.2	211.1	0.16
2	19.1	147.0	16.5	0.35
3	13.3	197.4	21.9	0.21
4	272.7	317.1	53.5	0.22
5	24.5	154.1	49.7	0.32
6	21.6	89.6	16.8	0.13
7	19.4	168.8	62.2	0.36
8	27.7	161.7	24.8	0.24
9	24.3	92.0	99.4	0.24
10	18.6	161.9	507.1	0.52
11	84.0	150.2	33.2	0.29
12	42.3	292.6	33.7	0.27
13	22.5	163.7	9.0	0.21
14	27.6	167.5	13.8	0.28
15	8.9	146.6	30.9	0.37

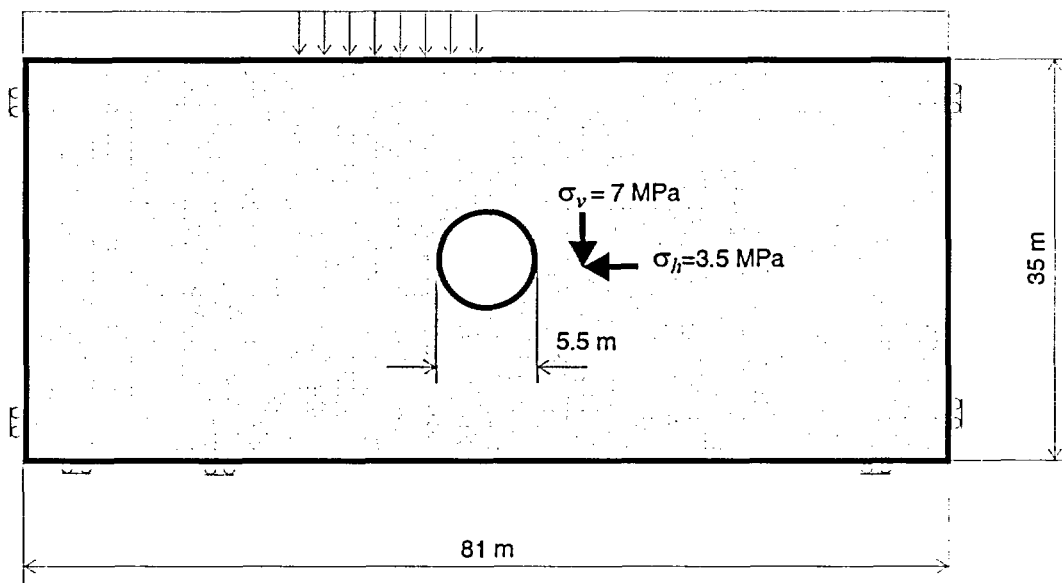


Figure 120. Thermal-Mechanical Model Initial and Boundary Conditions

The simulation was conducted for all six categories of the rock mass. It is observed that the amount of thermally induced rockfall is generally small. The temperature and stress fields for rock mass category 1 with the base-case thermal properties and 90 percent ventilation efficiency are shown in Figure 121. The figure shows the model state after 80 and 10,000 years of heating. There is no significant rockfall or damage induced by heating. Conditions are similar for other rock mass categories. Elastic stress paths during 10,000 years of temperature variation are

shown in Figures 122 and 123, for rock mass category 1 in the wall and roof, respectively, and in Figures 124 and 125, for rock mass category 5 in the wall and roof, respectively. The elastic stress paths confirm the results of the UDEC model. The drift wall in the category 1 rock mass is in the yielding state after drift excavation. Heating does not increase damage significantly (Figure 122). The stress state in the drift roof in category 1 (shown in Figure 123) moves closer to the yield surface during heating, but it still remains elastic. The thermal stress increase in the drift roof in the category 5 rock mass (Young's modulus of 19.7 MPa) moves the stress state barely above the yield surface (Figure 125) during the relatively short period of time when the temperature reaches the maximum, around 80 years after waste emplacement. This is consistent with observation of minor rockfall from the drift roof in rock mass category 5.

The rockfall simulations using temperatures from cases 2 and 3 of the thermal calculation do not show any increase in rockfall compared to the base case.

#### 6.4.1.3 Combined Seismic and Thermal Effect in Lithophysal Units

Stability of the emplacement drifts located in the lithophysal rock units was investigated for both thermal and seismic loading conditions independently for both seismic and thermal loading conditions in Sections 6.4.1.1 and 6.4.1.2, respectively. The initial condition for the seismic analysis discussed in Section 6.4.1.1 was in situ stress state perturbed by excavation of the drifts only. An additional analysis, presented in this section, was done to assess the effect of changing thermal stress in the rock mass around the repository after waste emplacement as an initial condition for seismic ground shaking. Using a similar approach as for the nonlithophysal rock (Section 6.3.1.4), stress paths during the regulatory period of 10,000 years were recorded at a number of locations around the drift. Temperatures from the thermal calculations for the base case and the sensitivity calculation for the heat removal ratio (case 3 in Section 6.2) were considered. The critical state was qualitatively determined from those paths, based on locations of stress states along that path relative to the yield surface. The critical state was used as an initial condition for the seismic analysis. Because the ground motion with  $1 \times 10^{-6}$  probability of annual occurrence results in complete drift collapse, it was not of particular interest to investigate the effect of that level of ground motion combined with thermally induced initial stresses. Instead, ground motion with  $5 \times 10^{-4}$  probability of annual occurrence was considered. Since the predicted temperatures are similar for the base case and the sensitivity case 2 at preclosure period, the sensitivity case 2 is not considered for the evaluation of the combined seismic and thermal effect. Rock mass categories 1 and 5 were considered in this analysis.

Stress paths (principal stresses) at 14 different locations around the drifts in rock mass category 1 during the regulatory period of 10,000 years are shown in Figures 126, 127, and 128. A yield condition corresponding to 10 MPa uniaxial compressive strength, and a selected friction angle of  $40^\circ$  is also indicated in the figures. Stress states at two points, almost at the drift springline (shown in Figures 126 and 127), are above the yield surface. Because those stresses are at the points inside the elastic blocks (inelastic behavior of this model is due to inelastic deformation of joints only), it is possible that they lay outside the yielding surface.

# Drift Degradation Analysis

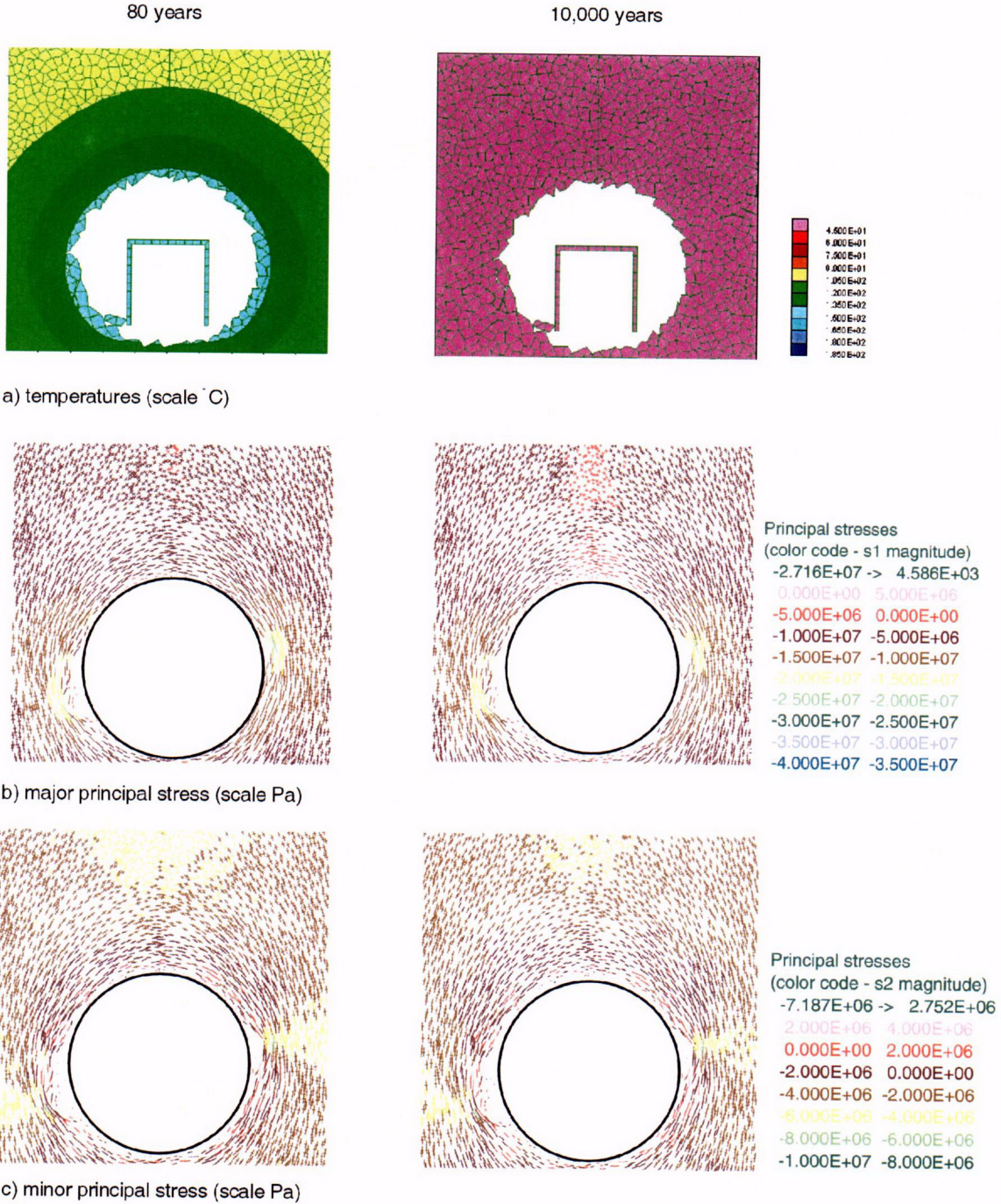


Figure 121. Thermally Induced Rockfall and Stresses After 80 and 10,000 years of Heating in Rock Mass Category 1

Drift Degradation Analysis

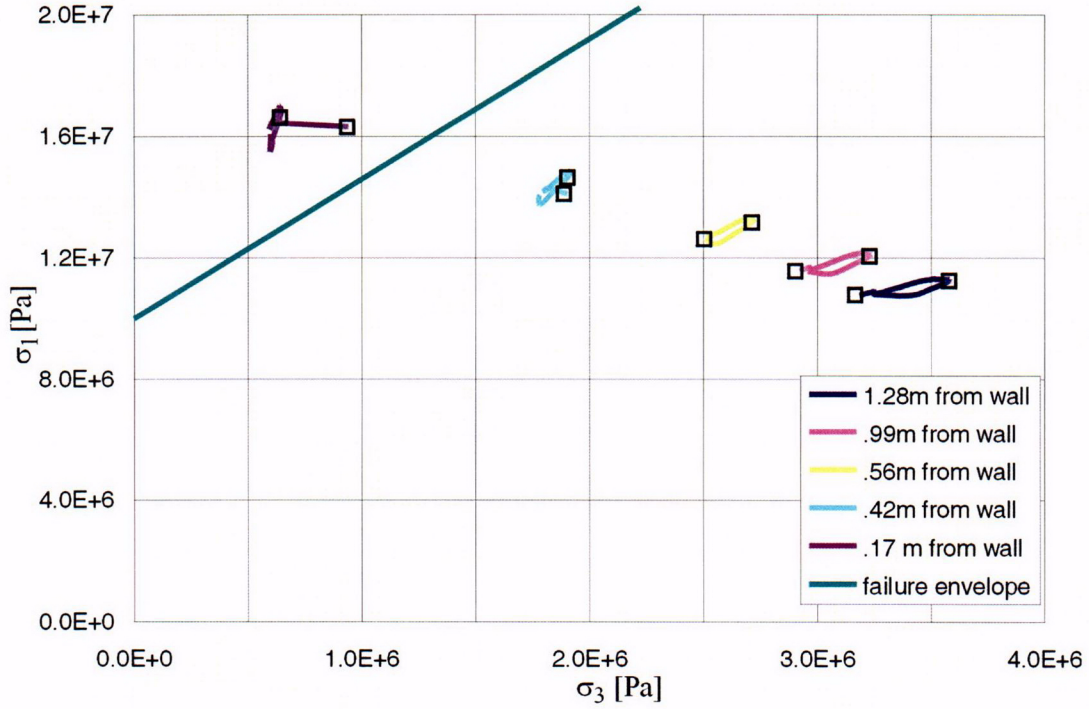


Figure 122. Elastic Stress Paths in the Drift Wall due to Temperature History: Category 1

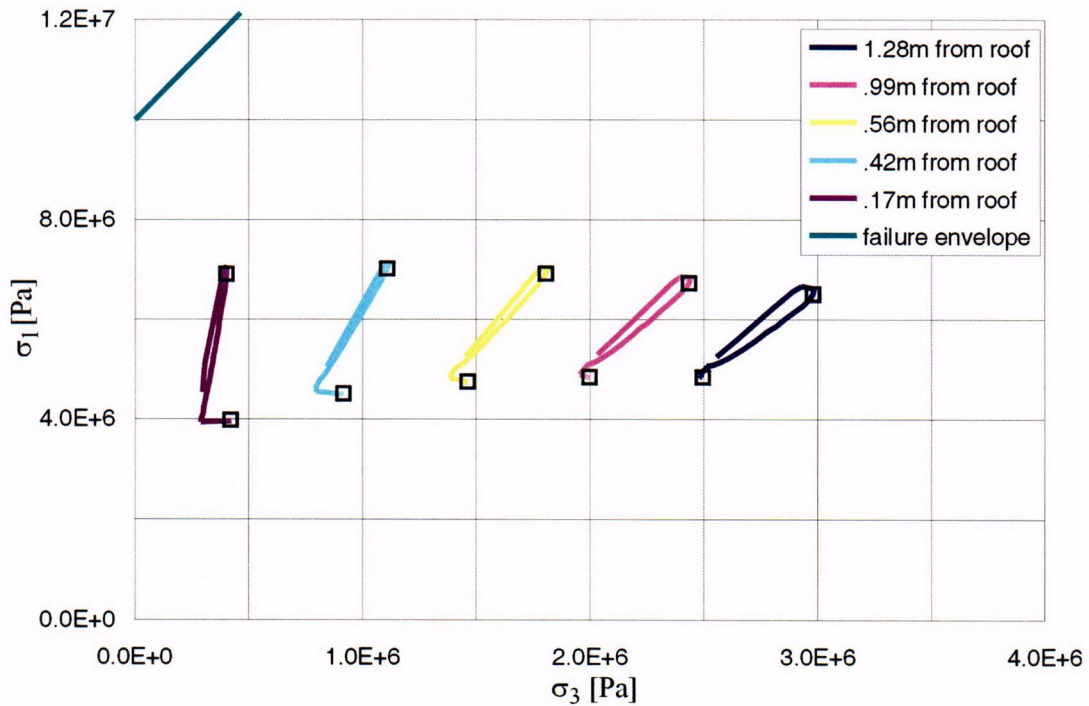


Figure 123. Elastic Stress Paths in the Drift Roof due to Temperature History: Category 1

Drift Degradation Analysis

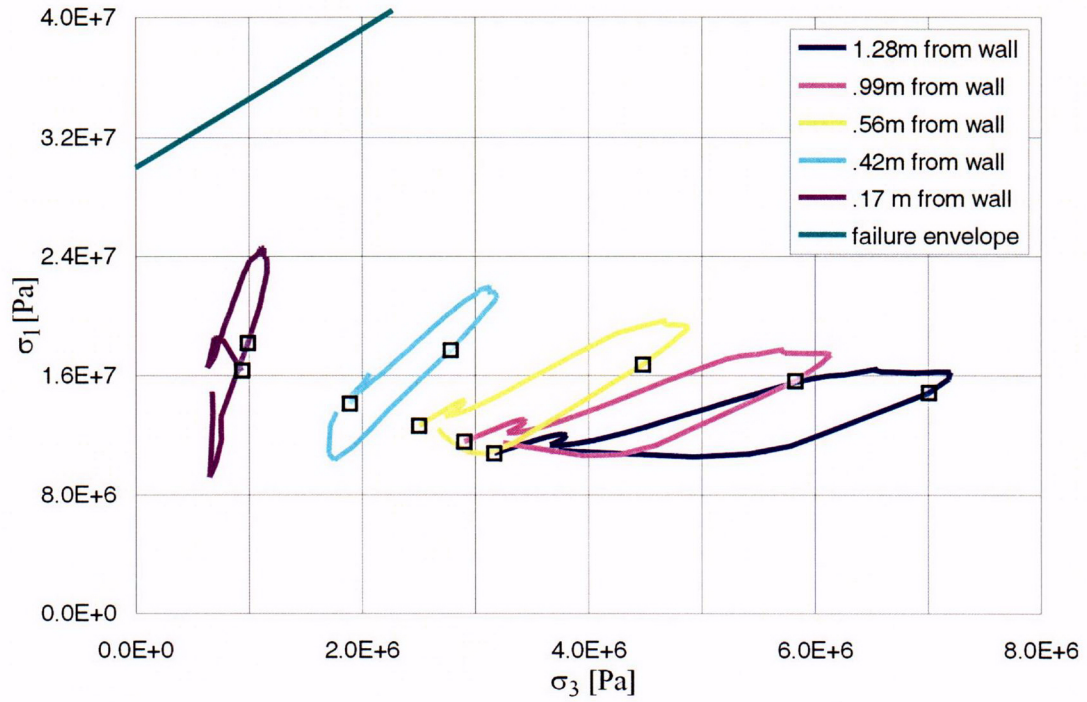


Figure 124. Elastic Stress Paths in the Drift Wall due to Temperature History: Category 5

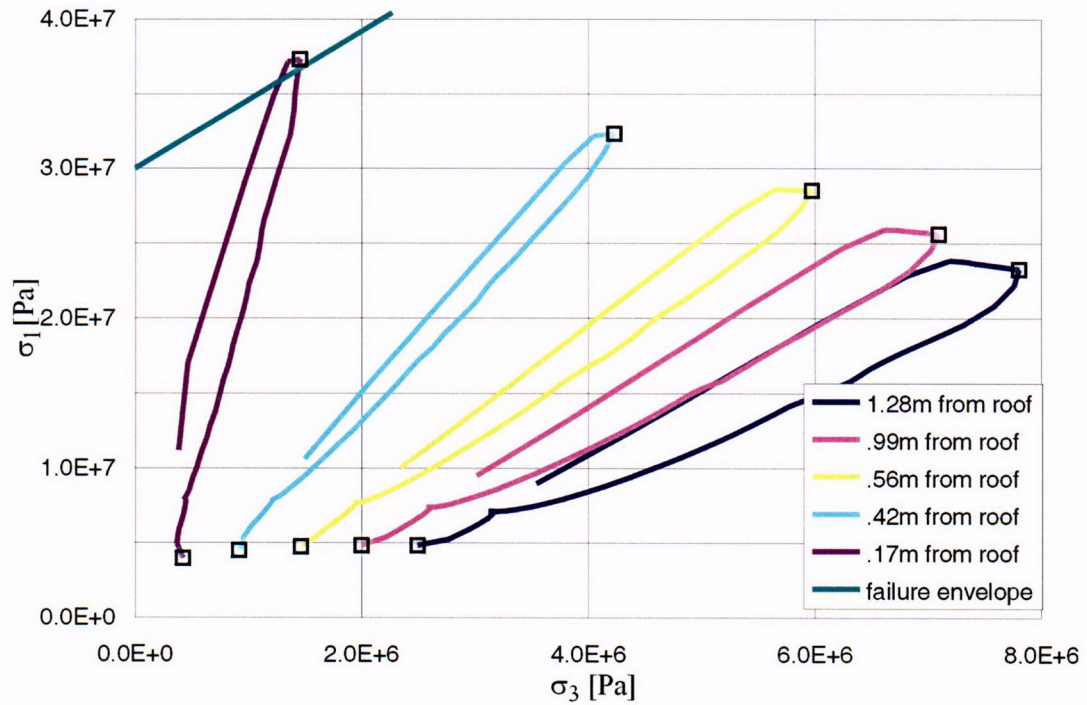


Figure 125. Elastic Stress Paths in the Drift Roof due to Temperature History: Category 5

Drift Degradation Analysis

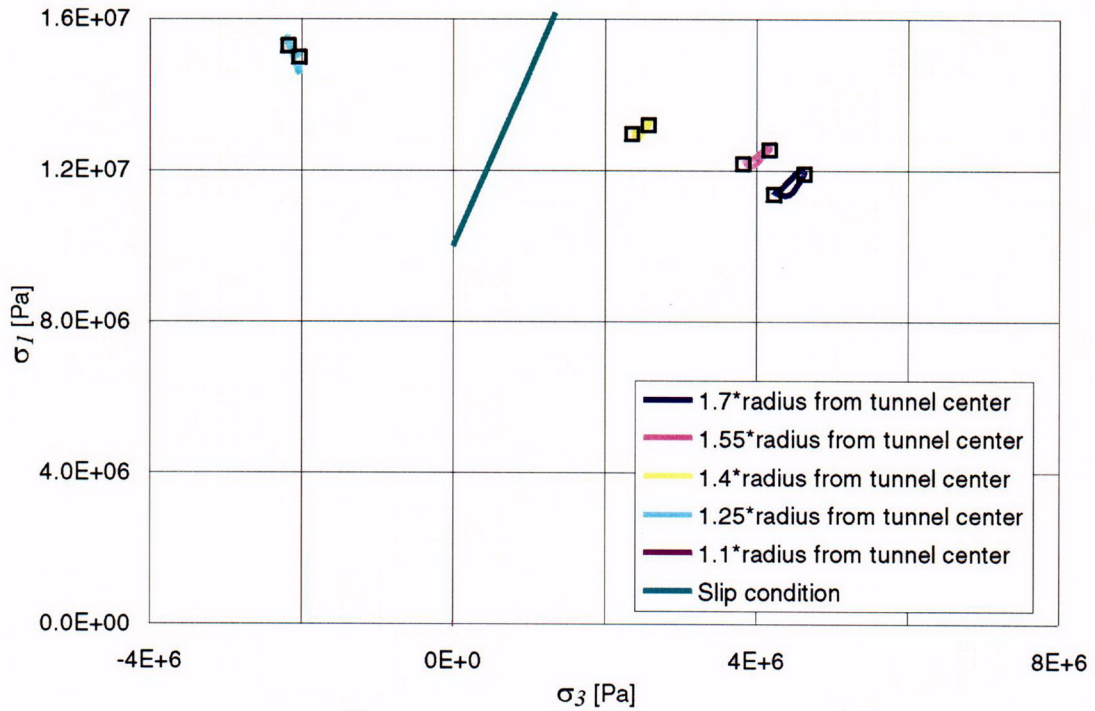


Figure 126. Stress Paths in the Left Drift Wall due to Temperature History: Category 1

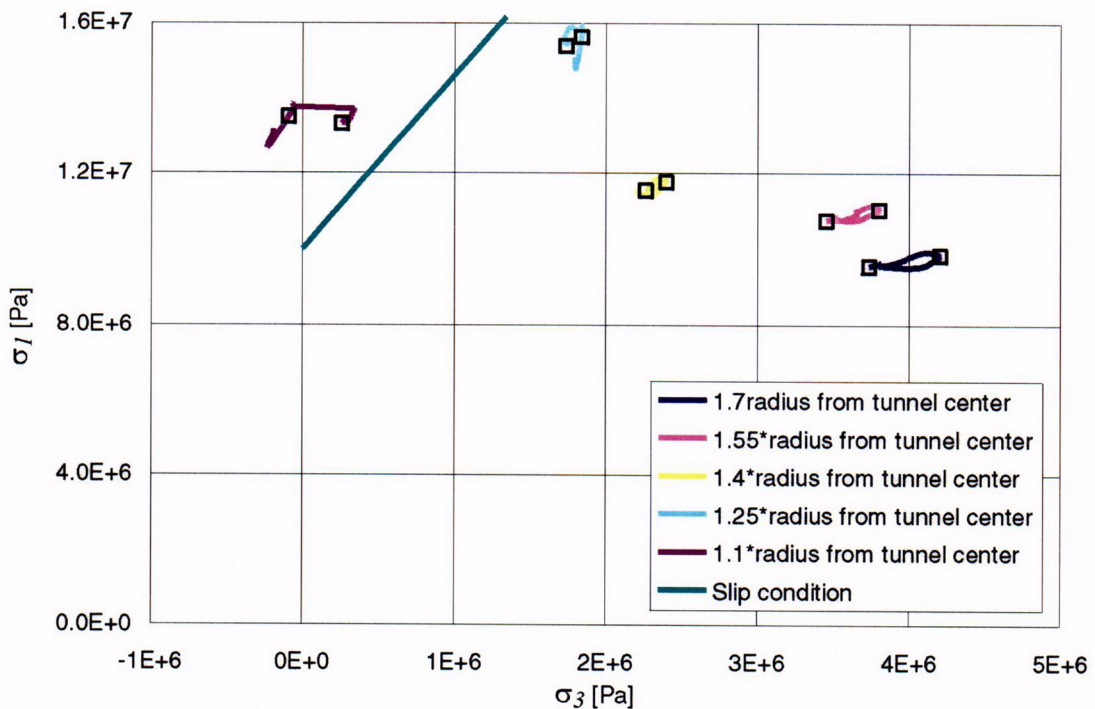


Figure 127. Stress Paths in the Right Drift Wall due to Temperature History: Category 1

Drift Degradation Analysis

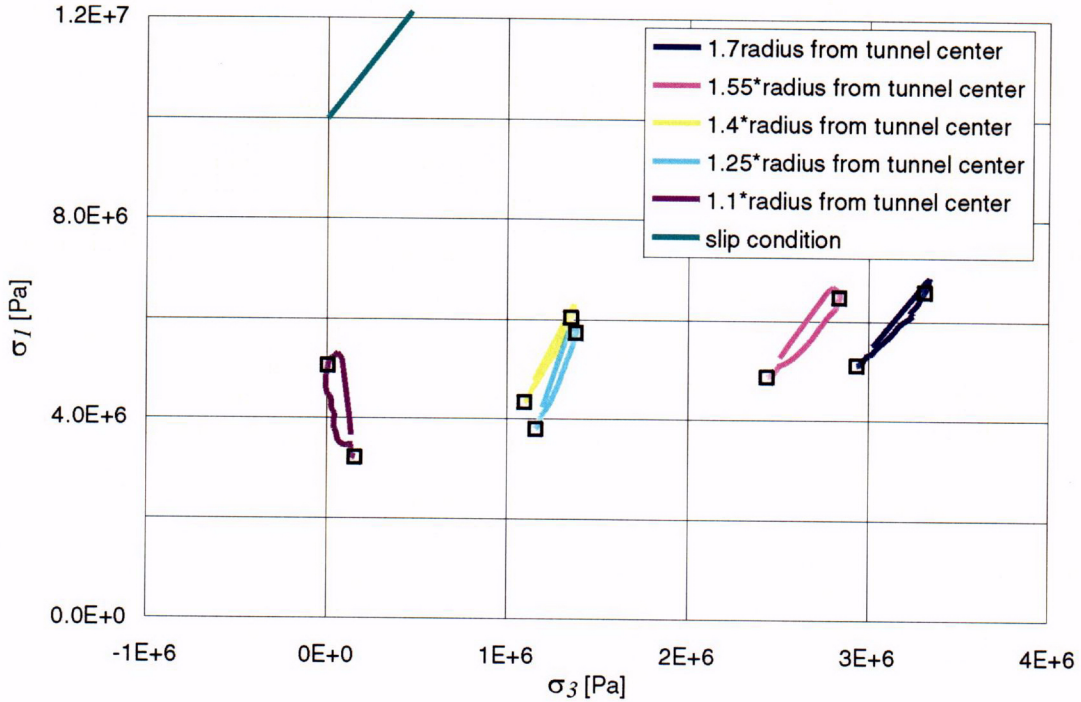


Figure 128. Stress Paths in the Drift Roof due to Temperature History: Category 1

Stress variation due to heating is quite limited in this case, since the stiffness of rock mass is small (i.e., Young's modulus is 1.9 GPa). The initial stress state and the state after 80 years of heating, selected as critical on the stress path, are marked on the plots with the squares.

Seismic analysis after 80 years of heating for rock mass category 1 resulted in an increased rockfall compared to rockfall from the seismic shaking of the rock mass at an in situ stress state (see Figures 129a and 130a). No rockfall is induced in rock mass category 5 in the case of 90 percent ventilation efficiency (Figure 129b), and very little rockfall in the case of 70 percent ventilation efficiency (Figure 130b). The result of an increase in rockfall for lithophysal rock mass category 1 is in an apparent contradiction with the results of the same analysis for the nonlithophysal units. Thermal stresses in the case of nonlithophysal rock resulted in reduced rockfall. However, the mechanism of rockfall is completely different for these two cases. In the case of the nonlithophysal rock mass, rockfall is due to sliding of blocks along the pre-existing joints, and an increase in the initial stress increases confinement on the joints, thereby increasing their resistance to sliding. In the case of the lithophysal rock mass, ground motion with  $5 \times 10^{-4}$  probability of annual occurrence causes rockfall by shaking down already damaged rock mass around the drift. Therefore, the heating induces additional damage (compared to damage caused by drift excavation), which does not necessarily result in a rockfall under static loading conditions, but is shaken down by the  $5 \times 10^{-4}$  ground motion.

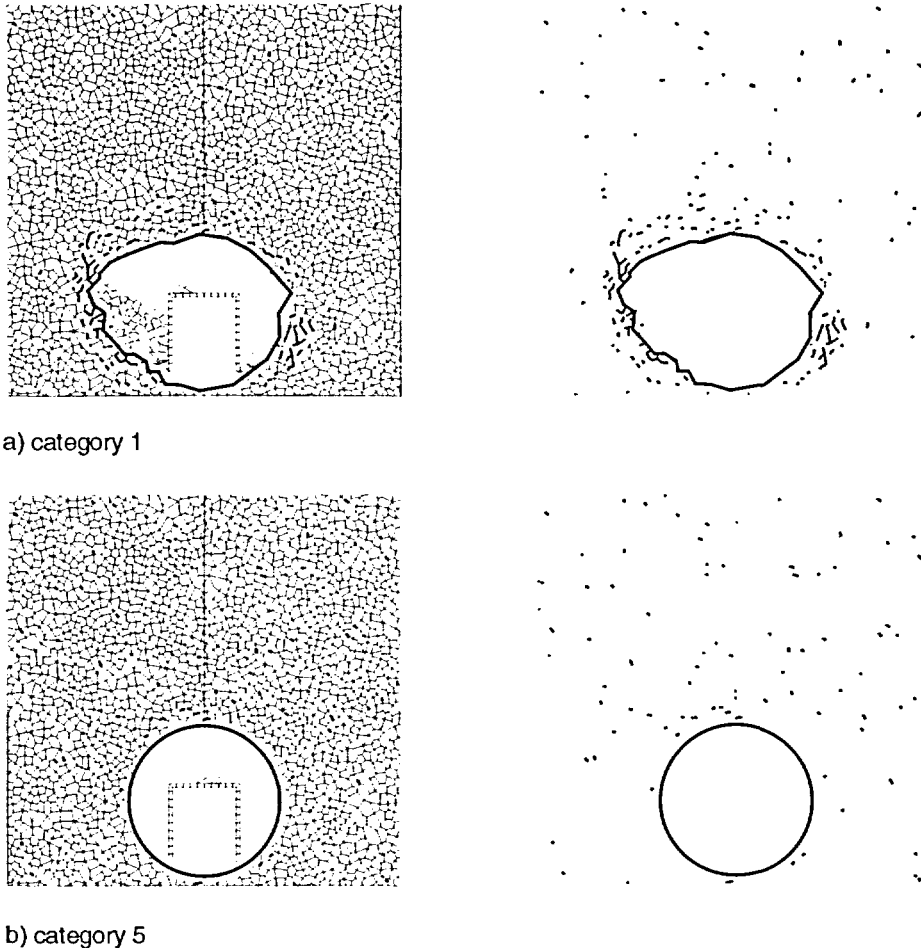


Figure 129. Rockfall and Fractures Induced Around a Drift by Preclosure Ground Motion After 80 Years of Heating in Rock Mass Categories 1 and 5

### 6.4.2 Lithophysal Rock Mass Degradation

Underground and surface excavations, which are designed to be stable after excavation, degrade with time, and some eventually collapse completely. The main reason for these observations is that strength of a rock mass exposed to humidity and temperature of the open atmosphere decays with time when it is loaded to a stress levels higher than 50 to 60 percent of its short-term strength. The rate of strength decay depends, among other parameters, on rock type, stress state, relative humidity and temperature. Stress corrosion is considered the main mechanism causing strength degradation of the rocks (Potyondy and Cundall 2001, Section 3).

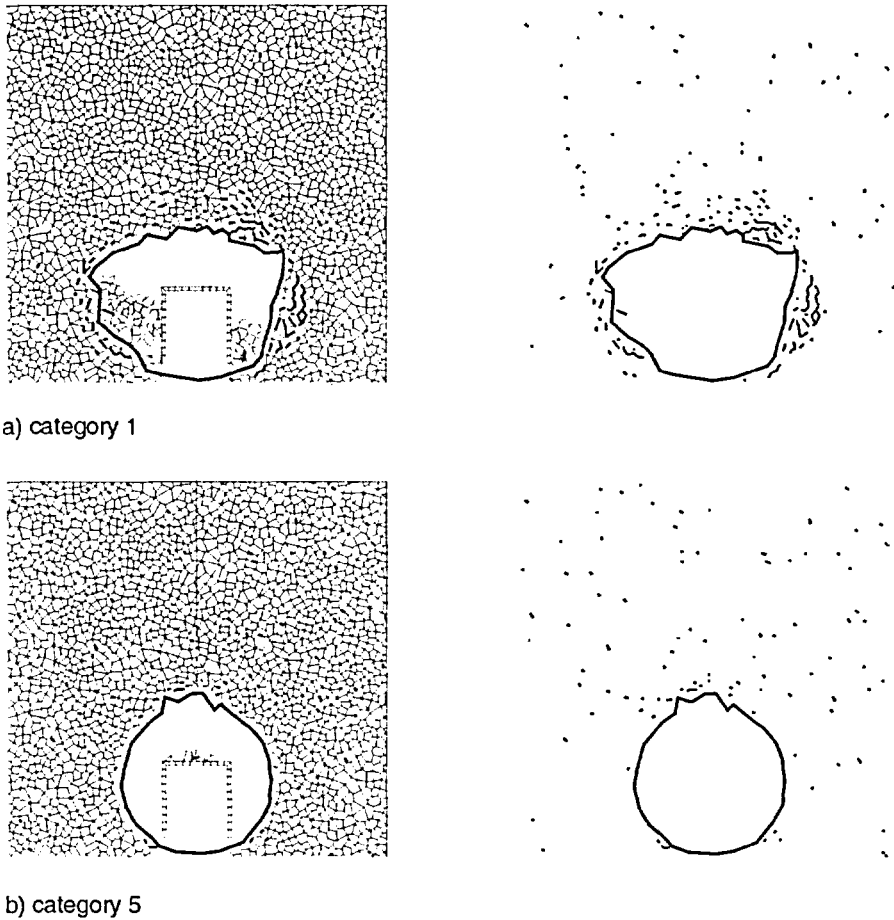


Figure 130. Rockfall and Fractures Induced around a Drift by Preclosure Earthquake after 80 Years of Heating (70 Percent Ventilation Efficiency) in Rock Mass Categories 1 and 5

The emplacement drifts at Yucca Mountain will be stable under currently existing conditions (in situ stresses and rock mass strength) without any ground support. However, it is expected that during the regulatory period of 10,000 years the ground support will completely lose its integrity, and drift degradation will occur due to strength decay of the rock mass. Drift degradation is important issue for the repository design and performance (e.g., drifts have to remain open during the preclosure period; the caved rock will load the drip shields possibly affecting their integrity and performance). Prediction of the rate of drift degradation for the duration of the regulatory period of 10,000 years is extremely difficult task (it requires extrapolation of testing results, which can be done for a period of months or a year, to a period of 10,000 years). Uncertainty in such predictions will be quite large. Although testing and modeling of strength decay of rock mass is recommended, it is reasonable to estimate the extent of caving of the rock mass above the drifts and the loads of the caved rock on the drip shield for the extreme conditions, when the rock mass completely loses its cohesive strength. Cohesion and tensile strength of the rock mass are considered to degrade to zero in the degradation model. Friction angle will likely have very minor change. No change of friction angle is considered in the model. Such an estimate will represent a conservative (i.e., high) upper bound of the load of the caved rock on the drip shield irrespective of the rate of strength decay and the residual strength of the rock mass.

Predictions of drift degradation and the load of the broken rock on the drip shield were done using three different approaches: (a) analytical, (b) numerical, continuum, and (c) numerical, discontinuum. Each of the methods uses certain conditions regarding caving of the rock above the drifts and transfer of the stresses within the broken rock mass. Those conditions make the model results (i.e., cave size and pressures on the drip shield) conservative in each of three approaches (i.e., the conditions result in higher pressures). The level of conservatism is the largest in the analytical results, and the smallest in the approach that represents rock mass as a discontinuum.

#### 6.4.2.1 Bulking

When the rock mass above underground openings collapses it increases volume (i.e., it bulks). During the collapse, either sudden or gradual, rock mass disintegrates in a number of pieces (blocks) which fall separately rotating along the way. When blocks equilibrate after caving, they do not fit together resulting in increased porosity and overall volume. Rock mass of volume  $V$  in the in situ conditions has volume  $V_B$  after caving, where:

$$V_B = (1 + B)V \quad (\text{Eq. 8})$$

where  $B$  is the bulking factor.

Amount of bulking (i.e., the bulking factor,  $B$ ) depends, among other things, on the lithology, pre-existing internal structure (jointing, bedding), and the mechanism of collapse. For example, density of crushed limestone is in the range between  $1360 \text{ kg/m}^3$  and  $1440 \text{ kg/m}^3$ , while density of the crushed dolomite is in the range between  $1280 \text{ kg/m}^3$  and  $1600 \text{ kg/m}^3$  (Fruchtbaum 1988). Considering that the specific gravity of limestones and dolomites is approximately 2.6 (Bauer et al. 1991), and using an in situ porosity of 20 percent (Goodman 1980), the in situ density of limestones and dolomites is approximately  $2200 \text{ kg/m}^3$ . Consequently bulking of these rocks from in situ state to a crushed state is between 37.5 and 72 percent. Duncan et al. (1980) reported that porosity of the rock fill for dams is between 23 and 36 percent. The rock fill used for dams is crushed to satisfy certain size requirement and is compacted during construction, which leads to reduction of its porosity. It appears from this discussion that bulking factor for the caved rock can be conservatively selected to be in the range between 0.2 and 0.4.

Caving of the underground excavations is a self-limiting process in many situations. At a certain stage of caving, due to bulking, the volume of the caved rock completely fills the volume of the original excavation and the volume occupied by the collapsed rock before onset of collapse. When the cave is completely filled, the broken rock provides the backpressure, which prevents further collapse of the rock mass.

#### 6.4.2.2 Analytical Consideration

It is considered in this approach that the cave above the emplacement drift grows until it becomes filled with the broken rock. The extent of the caved rock is calculated as a function of the bulking factor,  $B$ , considering that the cave stabilizes when it is completely filled with the broken rock. An additional unknown in this approach is the shape of the cave. Two extreme conditions illustrated in Figures 131 and 132 and were considered.

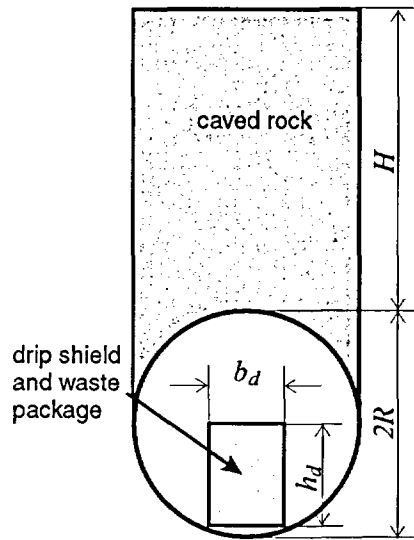


Figure 131. "Piping" Type of Caving Mechanism

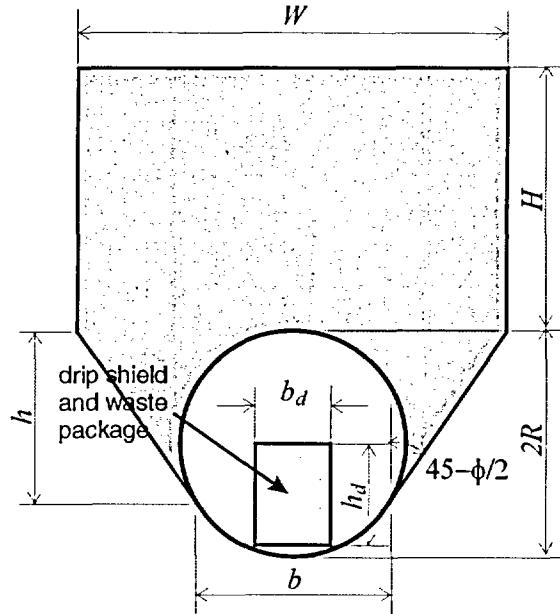


Figure 132. Terzaghi Type of Caving Mechanism

The "piping" mode of roof collapse (shown in Figure 131) is typical for conditions when the rock mass is bedded and there is a relatively large ratio of the span of the excavation to its depth. This type of roof collapse is typical for coal mines (with a bedded shale overburden) using the longwall mining method, and almost always occurs suddenly. Roof piping collapse is not a likely mode of drift collapse for the following reasons:

- None of the rock mass units are layered
- Drifts are relatively deep below the ground surface
- Drift collapse due to strength decay will evolve gradually over a long period of time.

The piping mechanism is considered here as a conservative extreme condition and is a mechanism that results in the largest vertical extent of the cave,  $H$ .

The other extreme condition of the rock mass collapse around the underground opening (shown in Figure 132) corresponds to the limit equilibrium conditions around a shallow tunnel, which Terzaghi (1943) used to calculate the load on the tunnel support. Slip lines extend from the drift walls at an angle of  $45 - \phi/2$  from the vertical direction, where  $\phi$  is the friction angle.

The cave height,  $H$ , is calculated for both cases as a function of the bulking factor,  $B$ . The pressure of the collapsed rock on the drip shield is calculated considering that the rock filling the cave acts on the drip shield as a dead weight. Expressions for the height of the cave are shown in Equations 9 and 10 for the piping and Terzaghi failure mechanisms, respectively, which have been derived based on the consideration of the geometry shown in Figures 131 and 132:

$$\frac{H}{2R} = \frac{1}{2} \left[ \frac{\pi}{2B} - \frac{b_d h_d}{2BR^2} - \left( 1 - \frac{\pi}{4} \right) \right] \quad (\text{Eq. 9})$$

$$\frac{H}{2R} = \frac{\frac{\pi}{B} - \frac{b_d h_d}{BR^2} - \frac{b+W}{2R^2} h + \frac{V_s}{R^2}}{\frac{2W}{R}} \quad (\text{Eq. 10})$$

where  $\frac{b}{R} = 2 \cos\left(\frac{\pi}{4} - \frac{\phi}{2}\right)$

$$\frac{h}{R} = 1 + \sin\left(\frac{\pi}{4} - \frac{\phi}{2}\right)$$

(Eq. 11)

$$\frac{W}{R} = 2 \left\{ \cos\left(\frac{\pi}{4} - \frac{\phi}{2}\right) + \left[ 1 + \sin\left(\frac{\pi}{4} - \frac{\phi}{2}\right) \right] \tan\left(\frac{\pi}{4} - \frac{\phi}{2}\right) \right\}$$

$$\frac{V_s}{R^2} = \frac{3\pi}{4} - \frac{\phi}{2} + 2 \cos\left(\frac{\pi}{4} - \frac{\phi}{2}\right) \sin\left(\frac{\pi}{4} - \frac{\phi}{2}\right)$$

The predictions of the cave height are shown in Figure 133 for the range of bulking factors between 0.2 and 0.4. As expected, the cave height is larger in the case of the piping mechanism than in the case of Terzaghi failure mechanism. The cave height varies (for two considered cases and for the bulking factor in the range between 0.2 and 0.4) between approximately 1 and 2.5 drift diameters.

The vertical pressure of the broken rock on the drip shield is calculated from the following equation, also derived based on the consideration of the geometry shown in Figures 131 and 132:

$$p = (H + R - t) \frac{\rho g}{1 + B} \tag{Eq. 12}$$

where  $t$  is the height of the upper surface of the drift shield above the drift centerline. Calculated vertical pressure on the drip shield as a function of the bulking factor is shown in Figure 134.

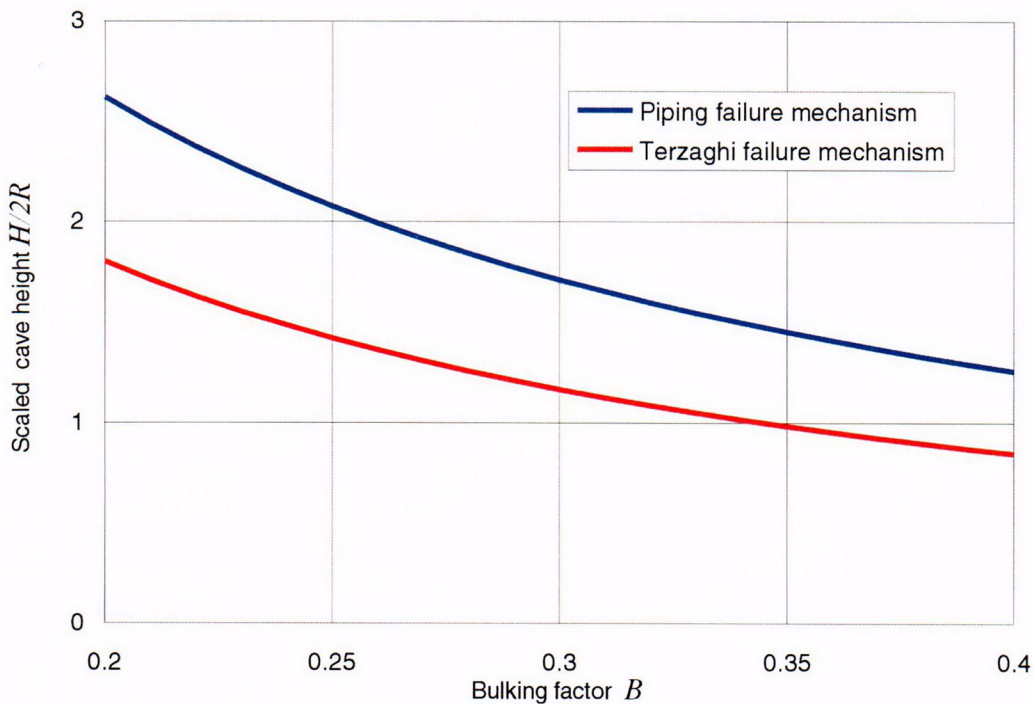


Figure 133. Cave Height as a Function of Bulking Factor: Analytical Solution

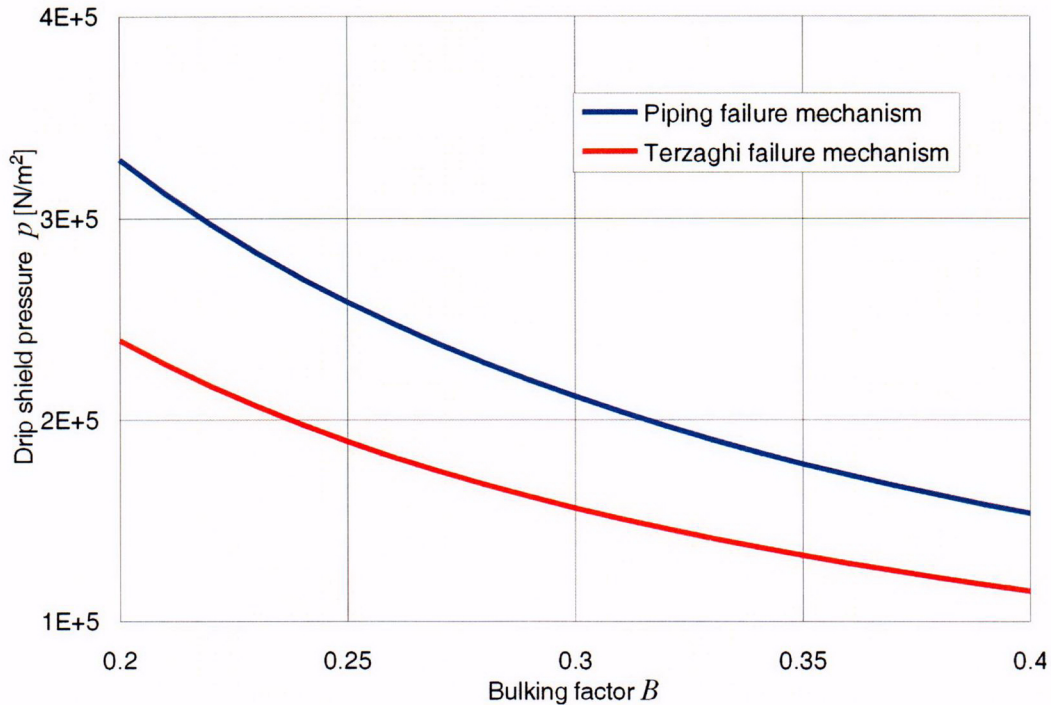


Figure 134. Vertical Load on the Drip Shield as a Function of Bulking Factor: Analytical Solution

#### 6.4.2.3 Numerical Continuum Approach

The purpose of the numerical analysis of the drift degradation and estimation of the pressures on the drip shield was to more accurately estimate the shape of the cave formed above the drift, and to account for potential stress arching within the broken rock piled on the top of the drip shield. A simplistic methodology was used. A model of the drift in the rock mass represented as a Mohr-Coulomb material was set using FLAC, a continuum numerical code. “Roller” boundary conditions were used on the vertical and the bottom model boundaries. A stress boundary condition was applied on the top model boundary. The model uses symmetry conditions along the vertical plane through the drift center. The model width was set equal to 10 drift radii. The total model height is either 16 or 25 drift radii, depending on vertical extent of the zone of the caved rock mass. The model bottom boundary is 4.8 radii below the drift center.

The actual strength of the lithophysal rock mass was used in the initial simulation (Table V-9, Category 1, with a friction angle of 40°). Subsequently, cohesion and tensile strength were reduced gradually, in steps. At each stage of strength reduction the model was run until either equilibrium was achieved, or there was clear indication that equilibrium could not be achieved (i.e., the rock mass around the drift was collapsing). Once the collapse was detected (an example is shown in Figure 135), the model simulation was interrupted, and the cave height was calculated based on the bulking factor and the volume of the rock mass within the destabilized region. Again, two limiting mechanisms were considered: 1) piping mechanism (shown in Figure 136, where the caved region is assigned zero cohesion), in which the cave width was limited to the drift width, and 2) Terzaghi mechanism (shown in Figure 137), in which cave width coincides with the width of the destabilized region of the rock mass. Subsequently the drift and the caved region were filled with zones (caved rock selected to have no cohesion or

## Drift Degradation Analysis

tensile strength, and density accounting for the bulking), and the model was run to the equilibrium to determine the load on the drift shield.

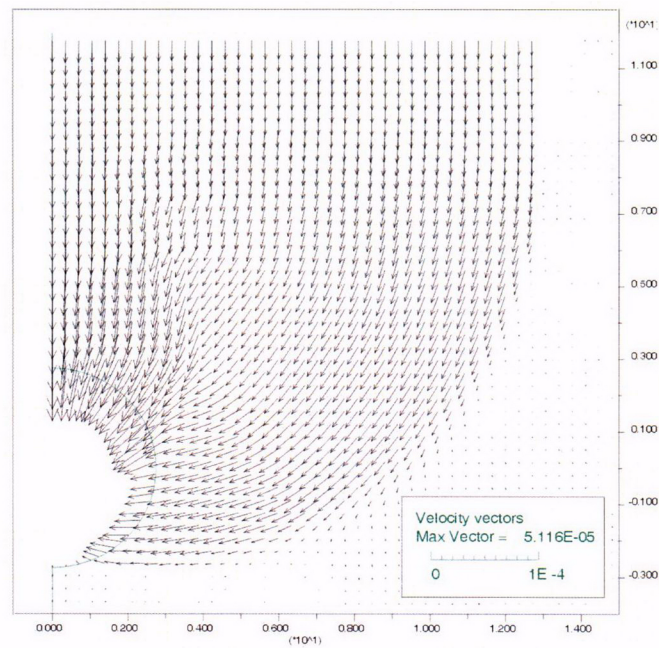


Figure 135. Failure Mechanism of a Deep Tunnel in Cohesionless Material

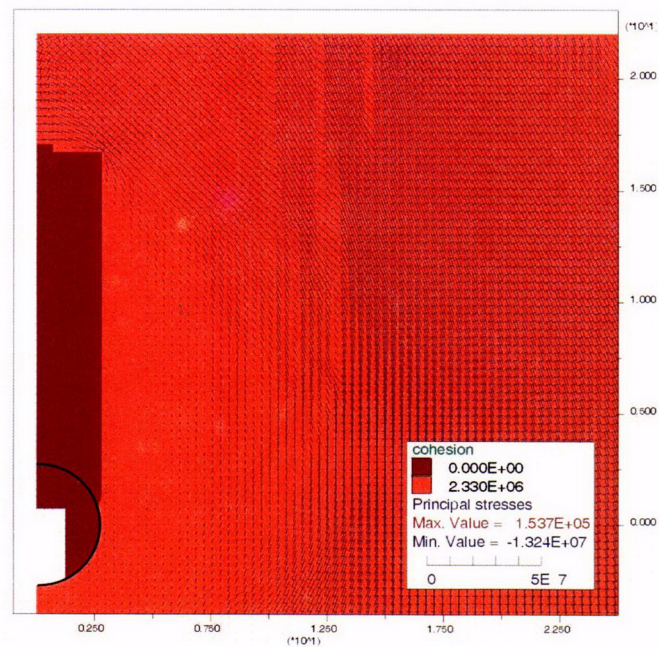


Figure 136. Piping Failure Mechanism Considered in the Continuum Model: Bulking Factor  $B = 0.2$

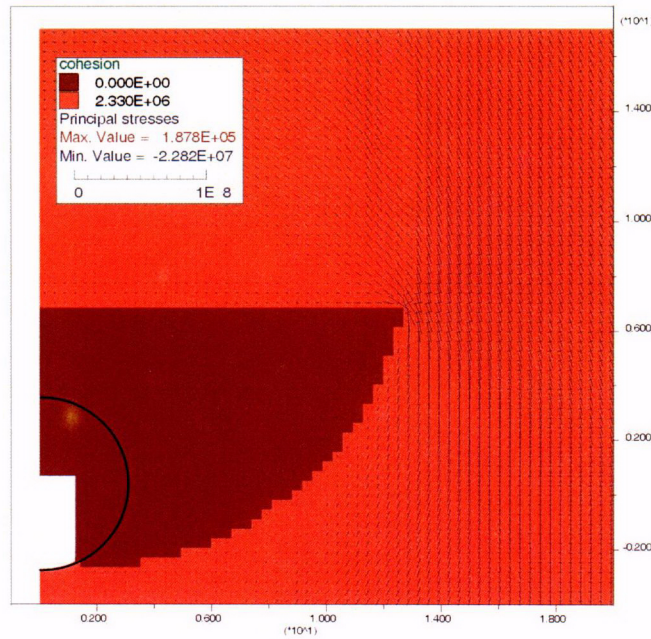


Figure 137. Terzaghi Failure Mechanism Considered in the Continuum Model: Bulking Factor  $B = 0.1$

Clearly, the failure mechanism shown in Figure 135 is not a realistic mechanism of the drift collapse at Yucca Mountain. This mechanism is more typical for the shallow tunnels in a soil-like media where shearing is the predominant mechanism of inelastic deformation. For emplacement drifts, collapse of the rock mass from the roof will occur much before the deep-seated shear failure in the walls can be mobilized.

Results of the continuum analysis of rock pressure on the drip shield as a function of the bulking factor and different failure mechanism types are summarized in Table 39.

Table 39. Summary of Pressures on the Drip Shield Calculated from the Continuum Model

Case	Property Category	Failure Type	Bulking	Pressure (kN/m <sup>2</sup> )	
				Top of Drip Shield	Side of Drip Shield
1	1	Terzaghi	0.1	269.2	47.1
2	1	pipe	0.1	403.3	39.6
3	1	Terzaghi	0.2	203.6	27.3
4	1	pipe	0.2	295.6	28.3
5	1	Terzaghi	0.4	117.9	20.1
6	1	pipe	0.4	161.6	17.8

#### 6.4.2.4 Numerical Discontinuum Approach

It appears that the results of both previously discussed approaches (analytical and continuum) are overly conservative in the predictions of the cavity size and transfer of the load through the caved rock. Consequently, predicted loads on the drip shield are quite large. Therefore, the problem was also solved using UDEC, a two-dimensional discontinuum numerical code. As in Section 6.4.1, the rock mass was represented as an assembly of polygonal blocks of a certain

shape (i.e., Voronoi blocks). The size and the shape of the blocks were selected such that it does not influence the results of the model. The same synthetic material as in Section 6.4.1, calibrated to macro properties of the rock mass (micro properties are shown in Tables 35 and 36), is used in the analysis of drift degradation.

The simulations started using the actual material strength. Cohesion and tensile strength were subsequently reduced in steps equal to 20 percent of the initial strength. For each step of strength reduction, the model was run to equilibrium allowing development of fractures and falling of any loose blocks. At the end of the simulation, when cohesion and tensile strength were completely reduced to zero, the model provides an estimate of the maximum extent of the collapsed rock mass and pressures on the drip shield. However, in this model the bulking of the caved rock is not a model parameter but its result. The bulking in reality depends on the size and the shape of the falling blocks, which are predetermined by the size and the shape of the Voronoi blocks in the model. To assure that the model estimates are conservative, the Voronoi block size was selected such that the resulted bulking factor was equal or less than 0.2, the lower bound of the bulking factor expected in rocks (cases 3, 4, and 5 in Table 40). The results of 5 simulated cases are summarized in Table 40. Cases 1 and 2 are for the model with a block size of 0.3 m, for different realizations of the geometry of Voronoi blocks. Cases 3, 4, and 5 are for different realizations of the geometry of 0.2-m large Voronoi blocks. Cases 1 and 2 resulted in a bulking factor of 37 and 30 percent, respectively. These values are within the expected range for the bulking factor of the rock mass, but cannot be considered as conservative. For that reason the analysis was done for a block size of 0.2 m (cases 3, 4 and 5). The resulting 16 to 17 percent bulking is certainly equal or less than the lower bound of bulking factor in rocks, yielding conservative (i.e., higher) estimates of the cave size and the pressure on the drip shield.

Table 40. Summary of Pressures on the Drip Shield Calculated from the Discontinuum Model

Case	Block Size (m)	Pressure (kN/m <sup>2</sup> )			Bulking
		Left Side of Drip Shield	Top of Drip Shield	Right Side of Drip Shield	
1	0.3	105.4	107.3	72.9	0.37
2	0.3	10.4	119.9	220.8	0.30
3	0.2	142.7	172.2	37.7	0.17
4	0.2	62.6	179.2	44.8	0.16
5	0.2	107.8	145.1	49.2	0.17

The pressures listed in Table 40 are averaged over two sides and the top of the drip shield. However the pressures are quite non-uniform as shown in Figure 138 for case 4. Note that the pressures shown in Figure 138 are forces averaged over 30 segments: 10 on each side and 10 on the top of the model. Details of drip shield pressures for each of the cases analyzed are provided in Attachment XVI.